A Framework for Energy Efficient UAV Trajectory Planning

Bruno Pereira de Carvalho

A Thesis

in

The Department

of

Electrical and Computer Engineering

Presented in Partial Fulfillment of the Requirements

for the Degree of

Master of Applied Science (Electrical and Computer Engineering) at

Concordia University

Montréal, Québec, Canada

September 2018

CONCORDIA UNIVERSITY

School of Graduate Studies

This is to certify that the thesis prepared

By: **Bruno Pereira de Carvalho**

Entitled: **A Framework for Energy Efficient UAV Trajectory Planning**

and submitted in partial fulfillment of the requirements for the degree of

Master of Applied Science (Electrical and Computer Engineering)

complies with the regulations of this University and meets the accepted standards with respect to originality and quality.

Signed by the Final Examining Committee:

_____ Chair
Dr. L.A.C. Lopes

_____ External Examiner
Dr. W. Lucia

_____ Examiner
Dr. R. Selmic

_____ Supervisor
Dr. L. Rodrigues

Approved by _____
Dr. W.E. Lynch, Chair
Department of Electrical and Computer Engineering

_____ 2018

_____
Dr. Amir Asif, Dean
Faculty of Engineering and Computer Science

Abstract

A Framework for Energy Efficient UAV Trajectory Planning

Bruno Pereira de Carvalho

Motivated by the reduced flight time of battery-powered UAVs, this thesis proposes a methodology for determining the optimal trajectories of a quadrotor in the sense of a trade-off between an energy-based cost and a time-related cost. Two main cost functionals are proposed to address the battery power consumption.

Firstly, a trade-off between costs associated with body acceleration and total time is studied for nonsteady maneuvers. An optimal state feedback solution that considers the nonlinearities of the quadrotor's equations of motion and the drag force components were developed. The main advantage of this technique is that it provides a state-feedback analytical expression.

Secondly, a simplified energy consumption model based on the blade element momentum theory (BEMT) is developed to deal with the cruise portion of the flight. The analytical solution for the constant altitude steady state flight minimum-energy problem was obtained and was similar to the maximum range problem solution. Based on the nature of the solutions, a hypothesis of a geometrical bound for the optimal pitch angle is raised.

The problems are formulated as a free terminal time optimal control problem using a trade-off cost index and solutions are derived using the Pontryagin's Minimum Principle (PMP). Simulations show the suitability of the proposed method.

Wahrlich es ist nicht das Wissen, sondern das Lernen, nicht das Besitzen sondern das Erwerben, nicht das Da-Seyn, sondern das Hinkommen, was den größten Genuß gewährt.

[Indeed it is not knowledge, but the act of learning, not possession, but obtaining, not arrival, but the act of getting there, which grants the greatest enjoyment.]

(**Carl Friedrich Gauss, 1808**)

Acknowledgments

Firstly, I would like to thank my thesis advisor Dr. Luis Rodrigues for his invaluable advice, support, and helpful guidance during the course of my research. I would like to acknowledge MITACS for their financial support and WowWee Canada for both their financial and technical support, as well as access to their facilities.

I would like to express my gratitude to my labmates, Emily, Maxim, Mailis, Michael, Alex, Julia, Reza, Amir, Inma, and Diego, for making a creative and fun environment where discussions were stimulated and opinions genuinely respected. A special thanks to all members of the UAV Concordia team for making me part of a group in which ideas are enthusiastically pushed forward.

Last but not least, I wish to thank my family and my close friends whose enthusiasm, interest and, support in this project have given me the motivation to realize this achievement. I would like to extend a very special thanks to my love for her companionship and encouragement.

Contents

List of Figures

List of Tables

List of Symbols

C_I	Cost index, m^2/s^4 or $N^{3/2}$
C_T	Thrust coefficient
C_M	Torque coefficient
C_t	Time-related costs, $\$/s$, or dollar per second
C_q	Cost of the battery charge, $\$/C$, or dollar per coulomb
D	Body drag, N
K	Body drag coefficient
g	Gravitational acceleration, m/s^2
H	Hamiltonian, kg/s or A
z	Altitude, m
$\dot{q}$	Battery current, A
J	Total flight cost, m/s or C
J_x	Partial derivative of the cost J with respect to the variable x, $1/s$
J_z	Partial derivative of the cost J with respect to the variable z, $1/s$
J_x	Partial derivative of the cost J with respect to the variable v_x, $1/s^2$
J_z	Partial derivative of the cost J with respect to the variable v_z, $1/s^2$
J_θ	Partial derivative of the cost J with respect to the variable θ, $Joule/^o$
dL	Blade element lift, N/m^2
dD	Blade element drag, N/m^2
P_e	Electric power, W
P_o	Profile power, W

P_{ind} Induced power, W

P_p Parasite power W

P_{thrust} Power generating thrust, W

P_{total} Mechanical power, W

t Time, s

T Total Thrust, N

U_o Nominal battery voltage, V

Q_o Nominal battery capacity, mAh

m Mass, Kg

x Horizontal position, m

η Overall electromechanical conversion efficiency

ρ Air density, kg/m^3

Chapter 1

Introduction

1.1 Motivation

Unmanned Aerial Vehicles (UAVs) have grown in popularity in the last decades, climbing their way to leading technology in the traditional aviation industry. Being remotely controlled, they have the ability to reach places and accomplish tasks that would be more costly and/or timely if performed by human beings. Due to the realization of its business potential, unmanned aerial technology has been adopted across many industries, encouraging the research and development thereof.

A quadrotor unmanned aerial vehicle is a class of rotorcrafts characterized by a configuration of four propellers positioned in such a way that an antipodal pair of rotors counterbalances the torque of the opposite pair. Position and yaw can be controlled by changing the thrust of each propeller. Due to their versatility, quadrotors have been used in several fields in recent years. Applications can vary from aerial mapping, traffic and agricultural surveillance, to rescue operations and package delivery, to name a few.

Despite the increasing number of applications, rotorcraft vehicles are not the most energy efficient design choice since lift is delivered uniquely by the propellers at all times. Although alternative sources of energy, such as solar and hydrogen cells, had been introduced in UAVs, the ratio of power to weight continues to rule the total system efficiency. Thus, in order to accomplish promising new applications, in which longer distances are flown, battery-powered UAVs will need to overcome their reduced flight endurance issue.

1.2 Literature Survey

There have been several articles addressing the multirotor energy efficiency and flight endurance matters, mainly tackling these subjects from the design perspective. A substantial efficiency improvement in most of vehicle subsystems has been achieved in the past few years. The author in [1] presents a method to design optimum propellers in the sense of minimizing momentum losses. The influence of design aspects, such as propeller configuration, number of blades and rotors, frame dimensions and shapes, battery, on the UAV efficiency are investigated in [2], [3], [4], [5]. Authors in [6] propose a model that relates the chosen mass of rotorcrafts to their endurance. Reference [7] concludes that most of the power consumed by quadrotors at hover is due to the motors, while the remaining power is spent in electrical circuits. In addition, new strategies to expand the flight endurance have been proposed. For instance, [8] included a laser power beaming as an extra source of energy, [9] proposed a battery swapping system, while [10] developed and assembled a novel six-rotor design to carry payloads in narrow corridors.

Another way of looking at the flight endurance issue is by considering the question of how to fly a certain UAV in a more (or the most) energy-wise cost-effectively way. Answers to this problem have not been vastly investigated. In order to fill the gap in the literature, this thesis will focus on the quadrotor trajectory planning problem exploring algorithms whose main feature is the energy economy.

Motivated by the expansion of the air traffic, path optimization techniques for aircraft have started to be explored. A survey of the flight trajectory optimization problems for fuel propelled aircraft vehicles is presented in [11]. In civilian aviation, real-time flight planning algorithms are incorporated in a device named flight management system (FMS). A flight management system (FMS) runs algorithms that provide optimal trajectories dependent on a parameter called the cost index (C_I). The cost index weighs different sources of cost in a flight operation according to the flight mode. This parameter is entered by the pilot. In UAVs, path generation algorithms as part of a flight management system is a more recent idea [12], [13], [14].

The formulation of the trajectory planning problem for UAVs has evolved from the simple shortest path approach to complex optimization problems, such as minimum time [15], [16], [17], minimum snap [18], minimum derivatives [19], among others. Dynamic programming [20], Model Predictive Control (MPC) [21], and genetic algorithms [22][23], have been proposed to address signal constraints and feasibility [19], collision avoidance [24], nonlinearities [25], and multiple vehicle formation [24][26].

Trajectory generation for UAVs based on energy-related criteria has not been vastly addressed in the literature. A heuristic procedure is proposed in [27] to solve the Generalized Traveling Salesman Problem with Neighbourhoods (TSPN), addressing the energy consumption problem of a six-rotor aircraft. By estimating the available energy for the quadrotor mission, [28] proposes an adaptive mission planner by solving numerically a Mixed Integer Linear Programming (MILP) problem. Reference [29] derives a theoretical model on the power consumption of a fixed-wing UAV. It formulates a trajectory optimization problem and proposes a solution based on linear state-space approximation and sequential convex optimization techniques. The author of [30] solved analytically the unconstrained minimum kinetic energy trajectory generation problem for a quadrotor in level flight without considering drag effects.

An essential part of the minimum-energy trajectory generation problem is the formulation of a power consumption model. Reference [31] sets up and experiment in a wind tunnel to study the power consumption of a multi-rotor in the forward flight condition. Based on results of less than 10% of error, they conclude that static propeller measurements together with blade element simulations are sufficient to estimate the performance of a propeller in forward flight. A method to evaluate the energy consumption of a vertical take-off and landing UAV (VTOL) is proposed in [32]. Their approach combines blade element theory and a model of the wings to formulate an optimization problem that can be solved numerically. The authors in [33] develop a theoretical power consumption model for a multi-rotor vehicle in steady-state flight. Although their model neglects the influence of the wind speed, their experimental results show small errors.

Reference [34] determines trajectories for a quadrotor solving numerically an optimal control problem in the sense of minimizing a power consumption model which is related to the angular accelerations of the propellers. Based on the model obtained in [33], reference [35] proposes an

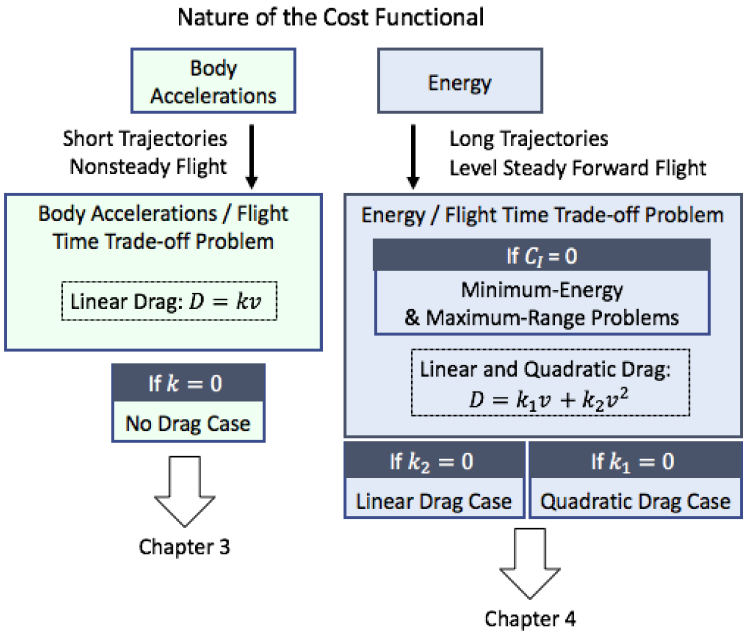

Figure 1.1: Thesis structure diagram

energy-based flight planning algorithm for traffic management system, in which routing algorithms are used to find optimal paths.

1.3 Contributions

The present work proposes a methodology for determining analytically the optimal trajectories of a quadrotor in the sense of a trade-off between a cost associated with the consumed energy and a time-related cost, which, according to the author's knowledge, has not been done before. Analytical solutions are particularly useful in real time algorithms for embedded systems, since they do not require a significant amount of computational power. In addition, this type of solutions usually provides helpful insights into the nature of the problem. The problems are formulated as a free terminal time-optimal control problems using a trade-off cost index and solutions are derived using the Pontryagin's Minimum Principle (PMP) [36]. This thesis contributes to the field of UAV trajectory planning as follows:

(1) An optimal state feedback solution for nonsteady flights that considers the nonlinearities of

the quadrotor's equations of motion and the drag force is developed in Chapter 3.

(2) Based on the blade element momentum theory, the formulation of an energy consumption optimal control problem of electric-powered quadrotors in steady forward flight at constant altitude is presented in Chapter 4.

(3) In Chapter 4, an analytical optimal solution for the minimum-energy problem in steady forward flight at constant altitude is obtained.

(4) A suboptimal solution for the energy consumption optimal control problem of electric-powered quadrotors in steady forward flight at constant altitude is obtained.

(5) From the geometrical interpretation of the solution proposed in Chapter 4, a range of efficient pitch angles for constant altitude steady forward flight where quadrotors should operate is obtained.

1.4 Thesis Structure

An overview of quadrotor modelling and important theories used later in this thesis are presented in Chapter 2. Furthermore, Chapter 2 provides a general overview of the theory used in the problem solution, namely optimal control theory. The problems formulated in this thesis are organized by their nature as shown in the diagram in Figure 1.1. Chapter 3 presents an optimal real-time flight management system for quadrotor UAVs that minimizes a trade-off between costs associated with body acceleration and total time. This general solution is then studied under the influence of body drag. Simulation results are provided for situations where the drag effect is considered. A flight management economy mode system is presented in Chapter 4 for long steady forward flights. Simulation results and the geometric interpretation of the solution are also provided. Conclusions and possible extensions of this work are then discussed in Chapter 5.

1.5 Published Work

Most of the work of Chapter 3 has been published in [37]:

B. Carvalho, M. Di Perna, L. Rodrigues, "Real-Time Optimal Trajectory Generation for a Quadrotor UAV on the Longitudinal Plane," in *European Control Conference*, June 2018, Limassol, Cyprus, pp. 3132-3136.

Chapter 2

Review of Modelling and Optimal Control

The first part of this chapter presents an overview of quadrotor modeling and the notation used throughout this thesis. A summary of optimal control theory is introduced in section 2.2.

The subscript notation is used for partial derivatives, i.e., L_a is short for the partial derivate of the function L with respect to the variable a. Additionally, the time derivative of L, i.e. $\frac{dL}{dt}$, is often denoted by $\dot{L}$.

2.1 Quadrotor Modelling

Quadrotor models started to be vastly researched at the end of the last century having as starting point the consolidated work on helicopter aerodynamics. Nowadays, due to simplicity and cost, most of the developed quadrotors in the market, differently from the commercial helicopters, employ a fixed-pitch blade design. The following sections will summarize the main aspects of the fixed-pitch quadrotor model which are used in this thesis.

2.1.1 Frames of Reference and Rotation Representation

In order to formulate a dynamic model for a quadrotor two frames of reference are introduced according to the Figure 2.1. Due to the relatively small magnitude of the accelerations experienced

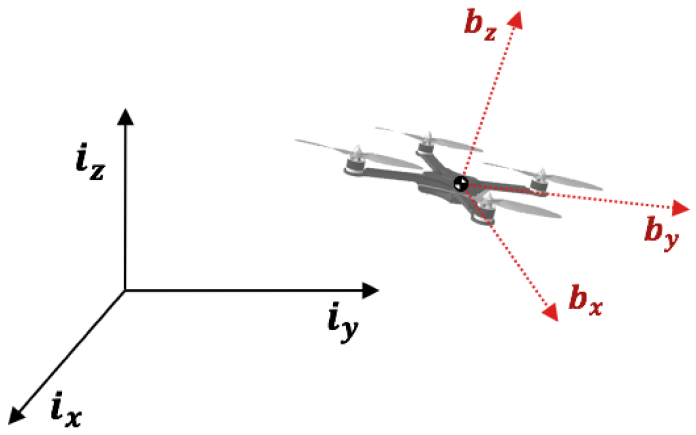

Figure 2.1: Frames of reference.

by the Earth, it can be accurately approximated as an inertial reference frame for the applications considered in this thesis. The inertial reference frame $\{\mathcal{I}\}$ has its base point I fixed on the surface of Earth. For a local area around the base point I, the Earth can be considered flat. The set $\{\mathbf{i_x}, \mathbf{i_y}, \mathbf{i_z}\}$ forms the basis vectors of $\{\mathcal{I}\}$, where the pair $\mathbf{i_x}$, $\mathbf{i_z}$ defines the longitudinal plane, with $\mathbf{i_z}$ pointing up. The point B, which coincides with the center of gravity of the quadrotor, and the set of basis vectors $\{\mathbf{b_x}, \mathbf{b_y}, \mathbf{b_z}\}$, which is aligned with the quadrotor principal axes of inertia, define the fixed-body reference frame $\{\mathcal{B}\}$.

Euler stated in the form of two theorems that two independent orthonormal coordinate frames may be related by less than four successive rotations about coordinate axes, where no two successive rotations may be about the same axis [38]. Additionally, the two independent orthonormal coordinate frames may be related by a single rotation about some axis. A rotation between the aforementioned two frames is usually described by one of the three representations: Euler angles, rotation matrices, or quaternions. The latter will not be revised in this document since it is not used in the scope of this work.

Rotation Matrices and Euler Angles

Let ${}^{I}[\mathbf{a}] \in \mathbb{R}^3$ be a point in three-dimensional space represented in the inertial coordinates and ${}^{B}[\mathbf{a}] \in \mathbb{R}$ be a representation of the same point expressed in the body-fixed coordinates. The

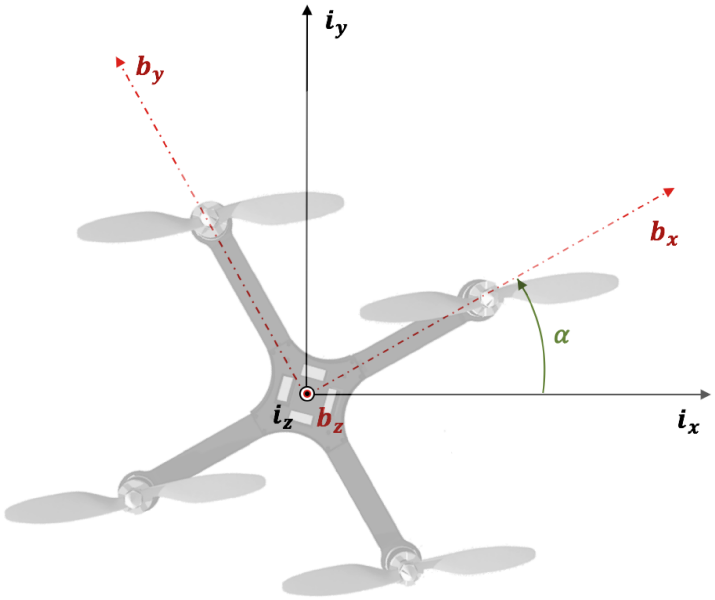

Figure 2.2: Rotation about z-axis.

following linear transformation then holds,

$$^{I}[\mathbf{a}] = {}^{I}_{B}R\,{}^{B}[\mathbf{a}], \tag{1}$$

where ${}^{I}_{B}R$ is called transformation matrix [39]. It is also possible to represent a single rotation about the third coordinate (z-axis) by

$$R_z(\alpha) = \begin{bmatrix} cos(\alpha) & -sin(\alpha) & 0 \\ sin(\alpha) & cos(\alpha) & 0 \\ 0 & 0 & 1 \end{bmatrix}, \tag{2}$$

where α is the angle of rotation according to the Figure 2.2. Similarly, one can write the same

transformation for the y and x-axes,

$$R_y(\alpha) = \begin{bmatrix} cos(\alpha) & 0 & sin(\alpha) \\ 0 & 1 & 0 \\ -sin(\alpha) & 0 & cos(\alpha) \end{bmatrix} \tag{3}$$

$$R_x(\alpha) = \begin{bmatrix} 1 & 0 & 0 \\ 0 & cos(\alpha) & -sin(\alpha) \\ 0 & sin(\alpha) & cos(\alpha) \end{bmatrix} \tag{4}$$

which complete one possible set of rotation matrices in the three-dimensional space. As a consequence, the result of subsequent rotations $R_y(\alpha_1)$ and $R_x(\alpha_2)$ of a vector $\mathbf{u}$ may be described by

$$\mathbf{u}' = R_y(\alpha_1)R_x(\alpha_2)\mathbf{u}. \tag{5}$$

Following Euler's theorems, one could find a parameterization where the rotation matrix $R_{zyx}(\phi, \theta, \psi)$ is the product of consecutive single rotations $R_z(\psi)$, $R_y(\theta)$, and $R_x(\phi)$, about the third, second, and first axes, respectively, i.e.,

$$R_{zyx}(\phi, \theta, \psi) = R_z(\psi)R_y(\theta)R_x(\phi) \tag{6}$$

where ϕ, θ, and ψ, are the so-called Euler angles or roll, pitch, and yaw, respectively. In addition, because $R_{zyx}(\phi, \theta, \psi)$ is orthogonal with determinant equal to 1, then $R^{-1}_{zyx}(\phi, \theta, \psi) = R^T_{zyx}(\phi, \theta, \psi)$. Finally, the relation of a vector ${}^I\mathbf{a} \in \mathbb{R}^3$ represented in the inertial coordinates and the same vector ${}^B\mathbf{a} \in \mathbb{R}^3$ expressed in the body-fixed system of coordinates is the following,

$${}^I\mathbf{a} = {}^I_B R^T(\phi, \theta, \psi)\, {}^B\mathbf{a} \tag{7}$$

where ϕ, θ, and ψ is one possible set of Euler angles from frame $\{\mathcal{I}\}$ to $\{\mathcal{B}\}$ (see Figure 2.3), and the bracket notation used in (1) as well as the subscript zyx are dropped for the sake of brevity. Similarly, the following expression holds

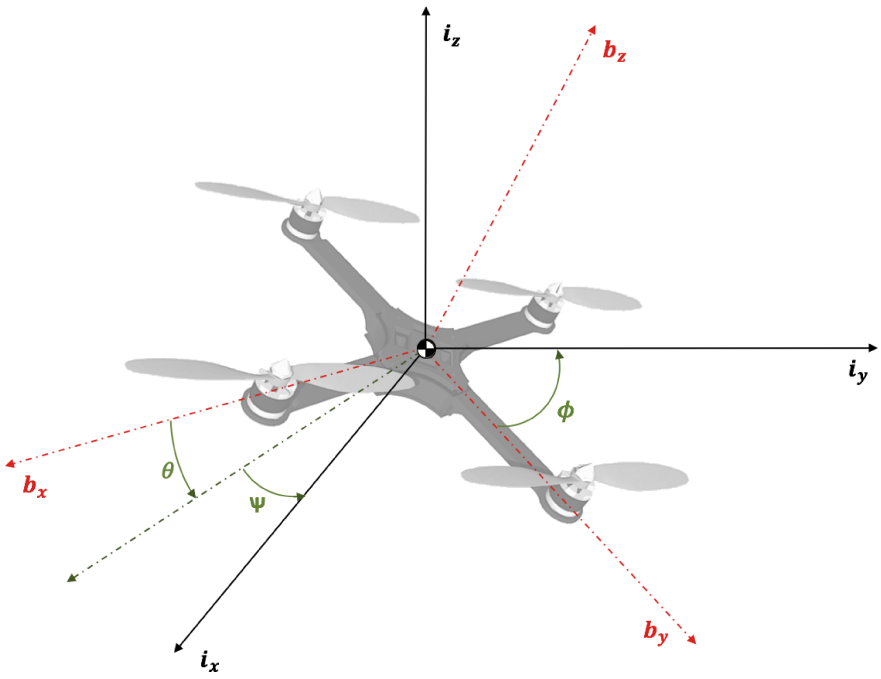

Figure 2.3: Euler angles.

$$ {}^{B}\mathbf{a} = {}^{I}_{B}R(\phi,\theta,\psi)\,{}^{I}\mathbf{a}. \tag{8} $$

In order to avoid singularities, the chosen set of Euler angles is assumed to satisfy the following interval.

$$ \phi \in (-\pi,\ \pi] $$
$$ \theta \in \big(-\frac{\pi}{2},\ \frac{\pi}{2}\big) $$
$$ \psi \in (-\pi,\ \pi]. $$

2.1.2 Rigid Body Dynamic Model

In order to formulate the quadrotor equations of motion, the following assumptions are made:

Assumption 2.1. *The quadrotor is a rigid body.*

Assumption 2.2. *The origin of the body-fixed frame $\{\mathcal{B}\}$ corresponds to the quadrotor center of gravity.*

Assumption 2.3. *The body-fixed frame coincides with the principal axes of inertia of the quadrotor.*

Assumption 2.4. *The quadrotor is considered to fly at altitudes where the ground effect is negligible.*

Assumption 2.5. *Wind disturbance is considered to be small and is neglected.*

Let the vector $\mathbf{x} = [x\ y\ z]^T$ represent the position of the quadcopter in the inertial frame $\{\mathcal{I}\}$ and the vector $\boldsymbol{\theta} = [\phi\ \theta\ \psi]^T$ be the rotation angles (roll, pitch, and yaw) from the inertial frame to the body-fixed frame. From Newton's second law of motion, the translational dynamics of a quadrotor can be described by the following second-order differential equation written in the inertial frame [40]

$$ {}^{I}\ddot{\mathbf{x}} = -g\mathbf{i_z} + \frac{1}{m}\,{}^{I}_{B}R(\boldsymbol{\theta})\ {}^{B}\mathbf{T} + -\frac{1}{m}\,{}^{I}\mathbf{D}(\dot{\mathbf{x}}, \boldsymbol{\theta}) \tag{9} $$

where g is the gravitational acceleration, m is the quadcopter mass, $\mathbf{D}(\dot{\mathbf{x}}, \boldsymbol{\theta}) = D_x(\dot{\mathbf{x}}, \boldsymbol{\theta})\mathbf{i_x} + D_y(\dot{\mathbf{x}}, \boldsymbol{\theta})\mathbf{i_y} + D_z(\dot{\mathbf{x}}, \boldsymbol{\theta})\mathbf{i_z}$ is the drag force acting at the center of gravity of the vehicle, $\mathbf{T} = T\mathbf{b_z}$ is the total thrust vector generated by the propellers, and ${}^{I}_{B}R(\boldsymbol{\theta})$ is the rotation matrix from the body-fixed frame to the inertial frame as described in (6).

Let $\boldsymbol{\omega} = \dot{\boldsymbol{\theta}}$ be the vector which represents the quadrotor angular velocity.From Euler's rotation equations, the rotational motion of a quadrotor is described by the following first-order differential equation,

$$ \mathbf{I}\dot{\boldsymbol{\omega}} = \mathbf{M} - \boldsymbol{\omega} \times (\mathbf{I}\boldsymbol{\omega}), \tag{10} $$

where $\mathbf{I}$ is the inertia matrix of the quadrotor,

$$ \mathbf{M} = \begin{bmatrix} l(T_1 - T_3) \\ l(T_2 - T_4) \\ M_1 - M_2 + M_3 - M_4 \end{bmatrix} \tag{11} $$

comprises the torques generated by the propellers (see Figure 2.4), and l is the quadrotor arm length. From the definition of principal axes, the inertia matrix can be represented in terms of its principal

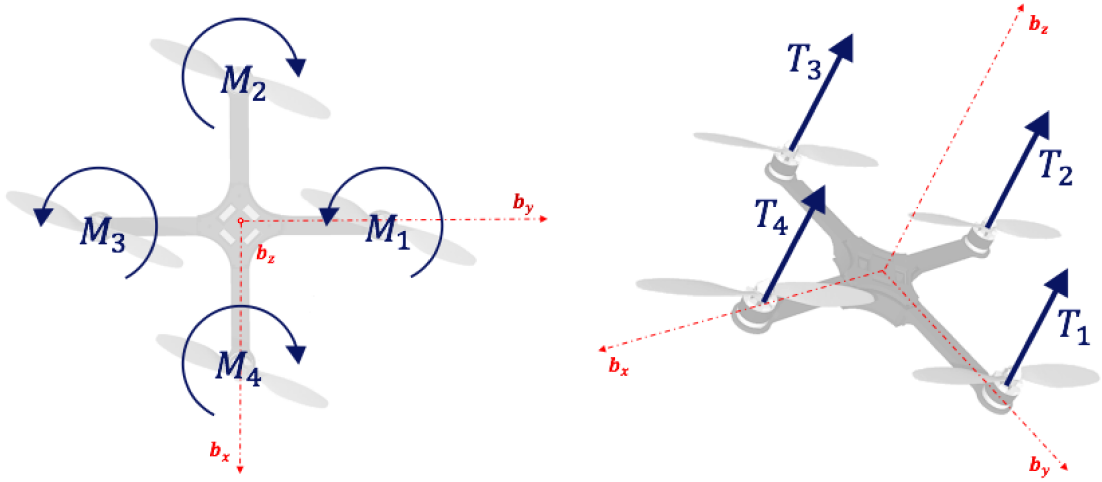

Figure 2.4: Thrust and torque convention

components in the body fixed frame

$$\mathbf{I} = \begin{bmatrix} I_{xx} & 0 & 0 \\ 0 & I_{yy} & 0 \\ 0 & 0 & I_{zz} \end{bmatrix}. \tag{12}$$

Expressions for the thrust T_i and torque Q_i, for $i = 1, ..., 4$, generated by each propellers are derived in the next sections.

2.1.3 Thrust and Torque

Blade Element Momentum (BEM) theory combines equations obtained from both blade element (BET) and momentum theories to estimate forces, torques, and power involved in a rotor-propeller system. This subsection adapts the derivations in [41] to the notation and framework used in this thesis.

Let $\mathbf{v} \in \mathbb{R}^3$ be the quadcopter velocity. Considering assumption 2.5, the apparent stream velocity into the rotor $\mathbf{V}$ has the same magnitude of $\mathbf{v}$ in the opposite direction. Let $\mathbf{v}_{ind} \in \mathbb{R}^3$ be the induced velocity caused by the acceleration of the air through the spinning rotor. For convenience, let the unit vector $\mathbf{b}'_\mathbf{z}$ be defined as $\mathbf{b}'_\mathbf{z} = -\mathbf{b}_\mathbf{z}$. At the rotor, the actual velocity is the sum of the two

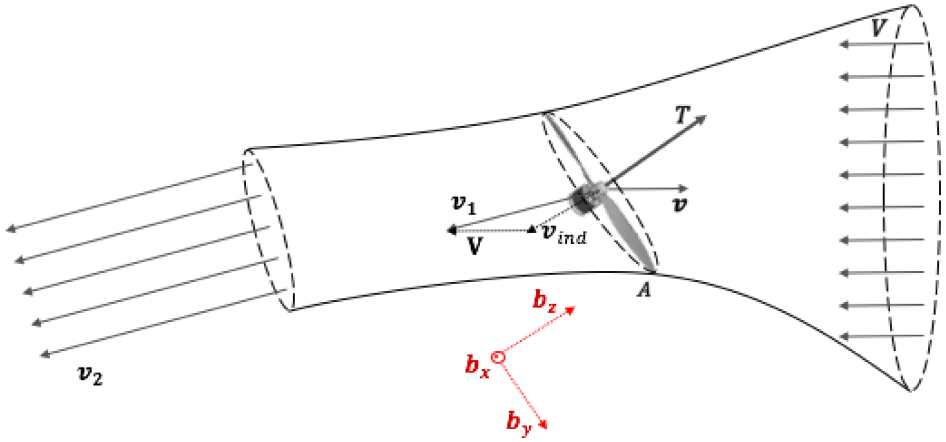

Figure 2.5: Rotor airstream control volume

aforementioned velocities,

$$\mathbf{v}_1 = \mathbf{V} + \mathbf{v}_{ind}. \tag{13}$$

Downstream, the air velocity in the far-wake region is $\mathbf{v}_2 \in \mathbb{R}^3$.

Momentum Theory

The following assumptions are considered.

Assumption 2.6. *The flow is considered to be steady, irrotational, inviscid and incompressible.*

Assumption 2.7. *Horizontal forces acting into the rotors are assumed to be very small for slow moving quadrotors.*

From Newton's law [42], defining a control volume delimited by the rotor disc A at the rotor hub in the axial direction as shown in Figure 2.5, the conservation of momentum at the upstream and downstream yields the following equation,

$$T = (\dot{m}_{air}\mathbf{v}_2 - \dot{m}_{air}\mathbf{V}).\mathbf{b}'_{\mathbf{z}} \tag{14}$$

where T is the magnitude of the thrust generated by one single propeller, and $\dot{m}_{air}$ is the mass flow

rate of the air through the control volume,

$$\dot{m}_{air} = \rho A |\mathbf{v}_1| \tag{15}$$

where ρ is the air density. The power generating thrust in a single propeller can be described by the

$$P_{thrust} = T\mathbf{v}_1.\mathbf{b}'_{\mathbf{z}}, \tag{16}$$

which is also described by the difference of the rate of kinetic energy in and out of the control volume,

$$P_{thrust} = \frac{1}{2}\dot{m}_{air}(\mathbf{v}_2.\mathbf{b}'_{\mathbf{z}})^2 - \frac{1}{2}\dot{m}_{air}(\mathbf{V}.\mathbf{b}'_{\mathbf{z}})^2. \tag{17}$$

Equating (16) and (17) and replacing the thrust term by (14), yields

$$\mathbf{v}_1.\mathbf{b}'_{\mathbf{z}} = \frac{\mathbf{v}_2 + \mathbf{V}}{2}.\mathbf{b}'_{\mathbf{z}}, \tag{18}$$

from the definition of the actual air velocity at the rotor ($\mathbf{v}_1$),

$$\mathbf{v}_{ind}.\mathbf{b}'_{\mathbf{z}} = \frac{\mathbf{v}_2 - \mathbf{V}}{2}.\mathbf{b}'_{\mathbf{z}}. \tag{19}$$

Finally, (19) and (15) can be plugged back into (14), which results in

$$T = 2\rho A |\mathbf{v}_1| \mathbf{v}_{ind}.\mathbf{b}'_{\mathbf{z}}. \tag{20}$$

Remark 1. *If the quadcopter is performing an axial motion ($\boldsymbol{V} = v_z\ \boldsymbol{b_z}$), and the induced air velocity occurs only in the axial direction ($\boldsymbol{v}_{ind} = v_{ind}\ \boldsymbol{b}'_{\boldsymbol{z}}$),*

$$T = 2\rho A(v_z + v_{ind})v_{ind}. \tag{21}$$

Remark 2. *If the quadcopter is hovering ($\boldsymbol{V} = 0$), and the induced air velocity occurs only in the axial direction ($\boldsymbol{v}_{ind} = v_{ind}\ \boldsymbol{b}'_{\boldsymbol{z}}$),*

$$T = 2\rho A v_{ind}^2. \tag{22}$$

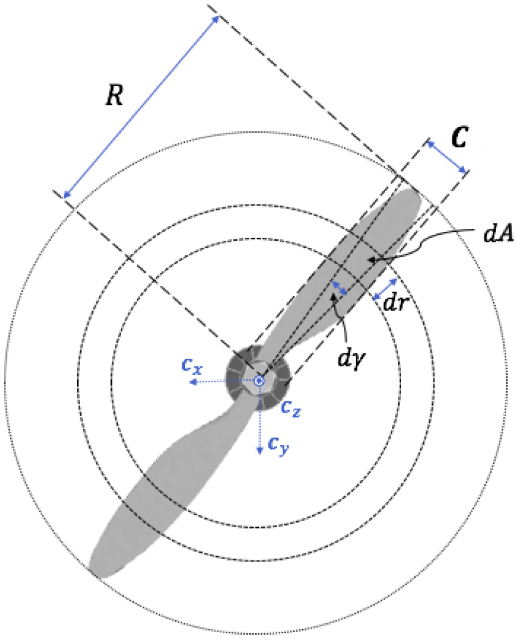

Figure 2.6: Blade element notation and rotating reference frame $\{\mathcal{C}\}$.

Blade Element Theory

The blade element theory (BET) intends to estimate the forces and torques acting on the rotor by integrating the infinitesimal components of these physical quantities along the blade azimuth (γ) and radius (r) directions (see Figure 2.6). Define each blade element by the coordinates (γ, r), expressed in the rotating reference frame $\{\mathcal{C}\}$ attached to the rotor, which spins at an angular velocity Ω. The aerodynamic lift $dL(r, \gamma)$ is the force perpendicular to the total airflow $\mathbf{v}_{total}(r, \gamma)$ on the blade element dA as shown in Figure 2.7. Similarly, the aerodynamic drag $dD(r, \gamma)$ is the force parallel to the total airflow on the blade element.

According to [43], it is possible to derive the following equations for the aerodynamical thrust and drag components on the blade element,

$$dL(\gamma, r) = \frac{1}{2}\rho|\mathbf{v}_{total}|^2 C_l \, dA \tag{23}$$

$$dD(\gamma, r) = \frac{1}{2}\rho|\mathbf{v}_{total}|^2 C_d \, dA \tag{24}$$

where C_d and C_l are the aerodynamical lift and drag coefficients.

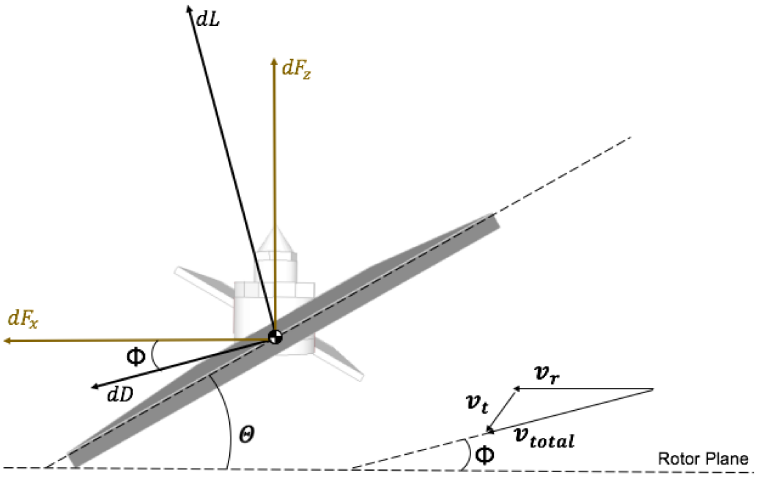

Figure 2.7: Blade element body diagram (longitudinal cut).

The total airflow on the blade element $\mathbf{v}_r(r, \gamma)$ can be broken down into two components. The first one represents the apparent speed due to the rotational motion of the blade, and it is parallel to the plane of the rotor. It can be shown that its magnitude is

$$|\mathbf{v}_r(r, \gamma)| = \Omega r. \tag{25}$$

The second component $\mathbf{v}_t(r, \gamma)$ appears due the translational motion of the rotor (or frame $\{\mathcal{C}\}$) plus the induced airflow. It can be seen from Figure 2.7, how the blade element force components relate to the lift and draft forces

$$dF_z(\gamma, r) = dLcos\Phi - dDsin\Phi \tag{26}$$

$$dF_x(\gamma, r) = dLsin\Phi + dDcos\Phi \tag{27}$$

where Θ is the blade angle, and Φ the angle between $\mathbf{v}_{total}$ and the rotor plane.

Slow moving rotorcraft UAVs typically perform forward flight maneuverers in a range of speed in between 0-20 m/s, and even slower axial motions. Additionally, rotors are commonly operating at higher at angular speeds than 1,000 rad/s. This fact leads to the following consideration.

Assumption 2.8. *For slow moving UAVs, the airflow on the element due to the translational motion is too small in comparison with the apparent wind velocity onto the blade element due to the rotor*

rotation, i.e. $|\boldsymbol{v}_t(r,\gamma)| << |\boldsymbol{v}_r(r,\gamma)|$*, then* $\boldsymbol{v}_{total}(r,\gamma) \approx \boldsymbol{v}_r(r,\gamma)$.

From the assumption 2.8, one can realize that the angle $\Phi \approx 0$. It is therefore possible to get the Taylor's first order approximation of expressions (32) and (33), which yields,

$$dF_z(\gamma, r) \approx dL - dD\ \Phi \tag{28}$$

$$dF_x(\gamma, r) \approx dL\ \Phi + dD. \tag{29}$$

For modelling purposes the following assumption is made.

Assumption 2.9. *The blade is a rigid body, azimuthally uniform, with constant chord length* C *and constant blade angle* (Θ) *along its radius* R.

From Assumption 2.9 that the blade element $dA(\gamma, r) = r\ dr d\gamma$ can be replaced by the blade element $dA'(r) = Cdr$, which is a rectangle of side C and infinitesimal height dr. This representation is valid since forces acting on different blade elements are approximately equal for different azimuths in the same r. Using equation (25) and Assumption 2.8, the expressions for the aerodynamical lift and drag in (23) and (24) for the blade element dA' can then be rewritten as

$$dL(r) = \frac{1}{2}\rho(\Omega r)^2 C_l\ C dr \tag{30}$$

$$dD(r) = \frac{1}{2}\rho(\Omega r)^2 C_d\ C dr. \tag{31}$$

It is possible to integrate the blade element quantities along r to obtain the thrust and torque generated by the rotor,

$$T = n_b \int_0^R F_z dr \approx n_b \int_0^R (dL - dD\Phi) dr \tag{32}$$

$$M = n_b \int_0^R F_x r dr \approx n_b \int_0^R (dL\Phi + dD) r dr, \tag{33}$$

where n_b is the number of blades in the rotor. Plugging (30) and (31) into (32) and (33), respectively, yields

$$T \approx n_b \frac{1}{6}\rho(C_l - C_d\Phi)\ C\ \Omega^2 R^3 \tag{34}$$

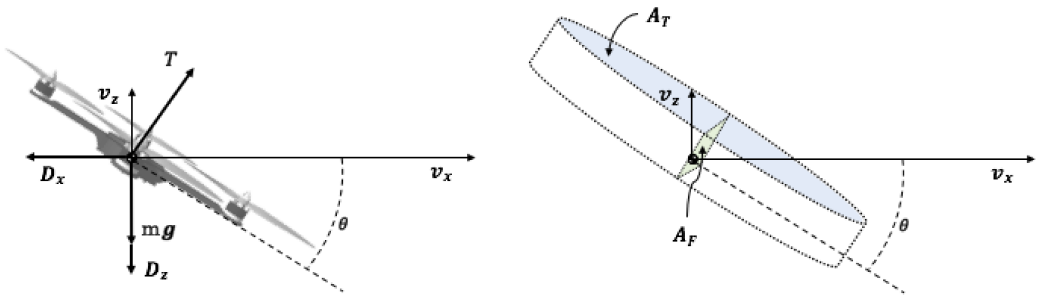

Figure 2.8: Aerodynamic drag model

$$M \approx n_b \frac{1}{8} \rho (C_l \Phi + C_d)\, C\, \Omega^2\, R^4. \tag{35}$$

All the parameters associated with the rotor geometry can be grouped together in one single constant.

$$T(\Omega) \approx C_T \Omega^2 \tag{36}$$

$$M(\Omega) \approx C_M \Omega^2, \tag{37}$$

where C_T and C_M are called thrust and drag coefficients, respectively. According to [44], the ratio between the ideal power to the real power of a rotor is called the figure of merit, which can be defined as,

$$FM = \frac{{C_T}^{3/2}}{\sqrt{2} C_M}. \tag{38}$$

2.1.4 Body Drag Force

The force generated by the relative airflow against the UAV in opposition to its translational motion is called drag. Below supersonic speeds, this effect is explained by three main different phenomena, each one having more influence in certain flight speed range. They are named form drag, skin friction drag, and induced drag. The sum of the form and the skin drag is called parasite drag (or aerodynamic). One way to model this type of effect in one dimension is by the following relation,

$$D_a = \frac{1}{2} \rho A C_d v_{rel}^2 \tag{39}$$

where A is the cross-sectional area, v_{rel} is the relative velocity between the vehicle and the wind, and C_d is the drag coefficient which depends on the vehicle shape and the Reynolds number [45].

Several models of the main types of drag on UAVs have been studied in [46], [47], [48], and [49]. In this thesis, the total drag effect on the longitudinal motion is modelled as,

$$\mathbf{D}(\dot{\mathbf{x}}, \boldsymbol{\theta}) = \mathbf{D}_a(\dot{\mathbf{x}}, \boldsymbol{\theta}) + \mathbf{D}_o(\dot{\mathbf{x}}, \boldsymbol{\theta}) \tag{40}$$

where, $\mathbf{D}_o$ is the drag vector that groups the influence of smaller drag terms, for instance, induced drag. For the longitudinal flight, the aerodynamic component of drag on the quadrotor is modelled as if it was acting on a cylinder. The right-hand side of Figure 2.8 shows this configuration, where A_T is the top area of the cylinder and the A_F is the largest cross-sectional area. This model yields the following expressions for the translational drag for a longitudinal flight,

$$D_{ax}(v_x, v_z, \theta) = \frac{1}{2}\rho C_d(A_T sin\theta + A_F cos\theta)v_x\sqrt{v_x^2 + v_z^2} \tag{41}$$

$$D_{az}(v_x, v_z, \theta) = \frac{1}{2}\rho C_d(A_T cos\theta + A_F sin\theta)v_z\sqrt{v_x^2 + v_z^2} \tag{42}$$

thus,

$$D_x(v_x, v_z, \theta) = D_{ax}(v_x, v_z, \theta) + D_{ox}(v_x, \theta) \tag{43}$$

$$D_z(v_x, v_z, \theta) = D_{az}(v_x, v_z, \theta) + D_{oz}(v_z, \theta) \tag{44}$$

In the literature, there are two approaches for modelling the total drag of flying vehicles. The first option is the adoption of a complex model that gathers most of the drag-related effects for rotorcraft vehicles. This approach often increases the complexity of the model to a level that it becomes unsuitable for study cases of even simple maneuvers such as forward flight. The second way is to look for relations of the type $\mathbf{D} = f_d(\dot{\mathbf{x}}, \boldsymbol{\theta})$ that suits observation data for a specific maneuver. Following one approach or the other one is a trade-off between the ability to predict the behaviour in a vast number of scenarios (flight modes) and the accuracy in a specific application. This thesis follows the second approach, and the following section will derive the total drag model

for two specific mode of operations.

Quasi forward flight mode

The quasi forward flight motion is adopted to study the nonsteady portion of the flight.

Definition 1. *On the longitudinal plane, the quasi forward flight mode is described as the condition in which a flying vehicle undergoes significant distances Δx in the horizontal direction while small vertical displacements Δz are performed for any interval of time $\Delta t > 0$ (see Figure 2.9), i.e. $v_x(t) >> v_z(t), \forall t$.*

It follows from the Definition 1 that the horizontal component of drag (D_x) is much larger than the vertical (D_z), for almost all time.

Assumption 2.10. *In the quasi forward flight regime, the vertical component of drag D_z is neglected.*

Assumption 2.11. *No aggressive maneuvers are performed, i.e., body accelerations are considered to be small.*

For the cases of Assumption 2.11, the pitch angle and the forward speed v_x are strictly related. It follows that the dependency on the orientation can be aggregated in the dependency on the forward speed, i.e.,

$$D_x(v_x, \theta) \approx D'_x(v_x). \tag{45}$$

In addition, because of the fact that the quasi forward flight mode will be used to describe slow trajectories (than in the steady portion), the Taylor's first order approximation can be used, and the total drag fits a linear model as in [50], [51].

$$D'_x(v_x) = kv_x, \tag{46}$$

where k is a positive constant to be determined experimentally.

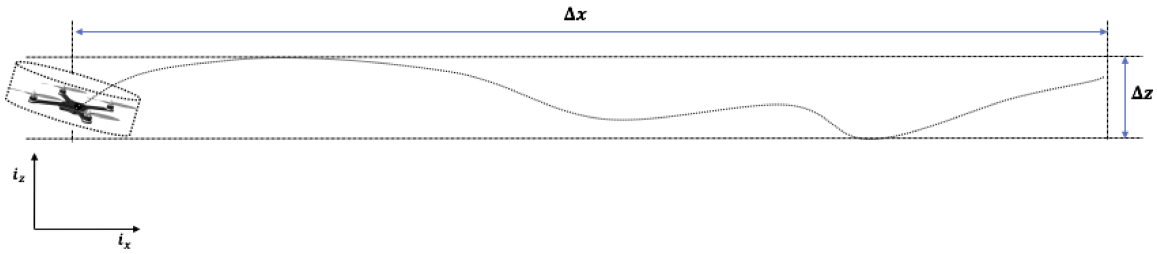

Figure 2.9: Quasi forward flight mode.

Constant altitude steady forward flight regime

Definition 2. *The constant altitude steady forward flight mode is described as the condition in which a flying vehicle performs a constant velocity motion in the horizontal direction while no vertical displacements are expected on the longitudinal plane. In that sense, the magnitude of the total drag force is equal to the total thrust projection in the horizontal direction, while the quadrotor weight balances the vertical projection of the thrust.*

In this case, only the horizontal component of drag exists (D_x). Note that from Definition 2,

$$D_x(v_x, \theta) = Tsin(\theta) \tag{47}$$

$$Tcos(\theta) = mg \tag{48}$$

which yields,

$$D_x(v_x, \theta) = mg\tan(\theta), \tag{49}$$

where θ is the forward flight pitch angle according to Figure 2.8. Because, the right-hand side of the above equation is constant in v_x and strictly monotonic in θ for the allowed interval $\theta \in (0, \pi/2)$, it can be shown that if $D_x(v_x, \theta)$ is stricly monotonic in v_x and θ, the solution of (49) can be parametrized by v_x. This result encourages the adoption of a relation f_d that is function of the forward speed only. Because velocities in steady flight are expected to be greater than in the nonsteady portion (at least for longer periods of time), the total drag is chosen to fit a quadratic model as in [52], [53],

$$D_{x_{steady}}(v_x) = k_1 v_x + k_2 v_x^2. \tag{50}$$

where k_1 and where k_2 are positive constants to be determined empirically.

2.1.5 Ideal Battery

LiPo (lithium polymer) is the most used type of battery in conventional quadrotors. It is preferable among alternatives, such as LiPo are nickel metal hydride (NiMH) and nickel cadmium (NiCd) batteries, due its high discharge currents and power density, The following assumptions will be made regarding the ideal model adopted for LiPo batteries which are similar to the ones made by [54] for lithium-ion batteries of a all-electric aircraft.

Assumption 2.12. *The internal resistance of the battery is small and will be neglected.*

Assumption 2.13. *The battery's output voltage (U_o) does not vary significantly with the state of charge (SoC), which means that the battery is considered to operate only in the nominal zone (central region of the discharge characteristic curve, Figure 2.10).*

Assumption 2.14. *Thermal effects are neglected.*

Assumption 2.15. *The battery capacity does not depend on the amplitude of the current.*

Under the above assumptions the electrical power delivered by the battery can be modelled as

$$P_e = -U_o \dot{q} \tag{51}$$

where U_o and q are the battery nominal voltage and charge, respectively.

2.2 Optimal Control

Although the development of optimal control theory got its maturity in the 20th century, few authors claim that its birth occurred way before, specifically in 1696 when Bernoulli posted the brachistochrone problem [55]. The primary objective of optimal control theory is to find inputs to control a dynamic system while optimizing a given performance index (or cost functional). Its principles find their utility, features, and application in many fields of science, for instance, biology, economics and business, computer, to cite a few. In engineering, optimal control methods such

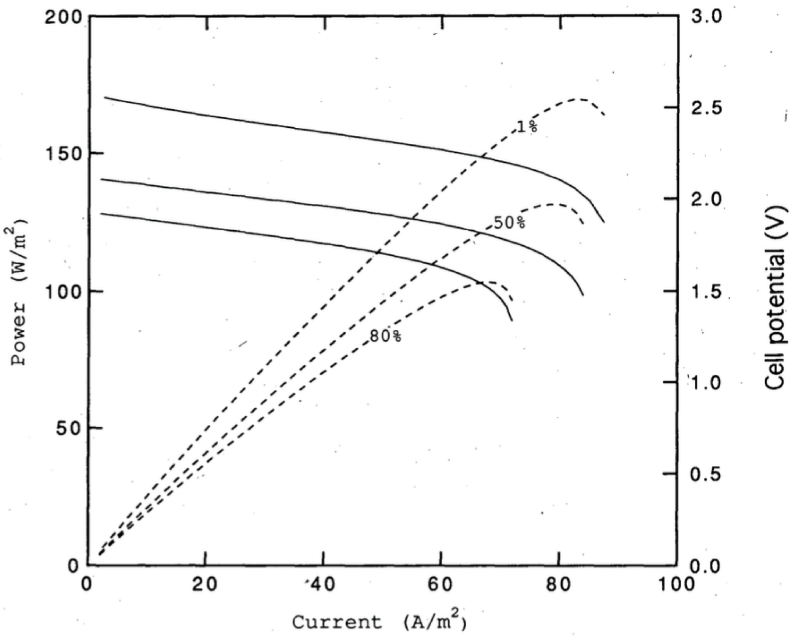

Figure 2.10: Power at 1, 50, and 80 percent depth of 2 discharge at the 3-hour rate (12.1 A/m^2) as a function of current density is shown by the dashed lines. Corresponding cell potential curves are depicted by the solid lines [Extracted from: Lawrence Berkley National Laboratory; Available in: https://escholarship.org/uc/item/61g2r55k]

as Pontryagin's Maximum Principle (PMP), are useful tools for formulating and solving real-life problems. Flight management system (FMS) algorithms relate closely to optimality principles. As a sub-case of FMS algorithms, the trajectory planning task of a UAV is considered one of the countless applications of this theory.

This section reviews a few topics on control theory. For further explanation on this material the reader is referred to [36], [55], [56], and [57].

2.2.1 Optimal Control Problem Formulation

In simple words, an optimal control problem (OCP) consists of a control system and an associated cost functional to be minimized.

Control systems are composed of system states, control inputs, boundary conditions, and constraints. When described in the continuous time domain, control systems are usually modelled by

differential equations of the form

$$\dot{\mathbf{x}}(t) = f(t, \mathbf{x}(t), \mathbf{u}(t)), \tag{52}$$

where $\mathbf{x}(t) \in \mathbb{R}^n$ represents the vector of system states, f is a $\mathcal{C}^1$ function (continuously differentiable), $\mathbf{u}(t) \in \mathcal{U}$ the vector of input variables, $t \in [t_0, t_f]$ is time, $\mathcal{U} \subset \mathbb{R}^m$ is the set of admissible control inputs, and n and m are the number of state and input variables, respectively. Moreover, $\mathbf{x}_f = \mathbf{x}(t_f)$ is the final state which is either fixed or free, and $\mathbf{x}_0 = \mathbf{x}(t_0)$ is the initial state. Finally, the final time t_f may be fixed or set free.

The cost functional introduces a penalty (or cost) associated with each system behaviour. Cost functionals are generally parametrized by the system states, inputs, and time variable. Because it is a real-valued function on a space of functions, this entity is a *functional*, usually denoted by the capital letter J, and it is of the form

$$J = \int_{t_0}^{t_f} L(t, \mathbf{x}(t), \mathbf{u}(t)) d\tau + K(t_f, \mathbf{x}_f), \tag{53}$$

where L, also called Lagrangian, is the running cost, and K is the terminal cost, both $\mathcal{C}^1$.

For the sake of readability, the function-of-time notation (t) is often suppressed for variables such as $\mathbf{x}$ and $\mathbf{u}$, and the optimal control problem is therefore formulated as

$$\begin{aligned} J^* = \inf \left\{ \int_{t_0}^{t_f} L(t, \mathbf{x}, \mathbf{u}) d\tau + K(t_f, \mathbf{x}_f) \right\} \\ s.t. \\ \dot{\mathbf{x}}(t) = f(t, \mathbf{x}, \mathbf{u}) \\ \mathbf{x}(t_0) = \mathbf{x}_0 \\ \mathbf{x}(t_f) = \mathbf{x}_f \\ \mathbf{u}(t) \in \mathcal{U}. \end{aligned} \tag{54}$$

2.2.2 Pontryagin's Maximum Principle

In order to analyze the OCP described in (54), the system dynamic equations (52) can be adjoined to the running cost L by the introduction of the time-varying vector of costate variables (or Lagrange multiplier) $\mathbf{J}_x^T(t) \in \mathbb{R}^n$. Additionally, this thesis considers the unconstrained OCP, meaning that $\mathcal{U} = \mathbb{R}^m$.

The following theorem states the maximum principle for the fixed-endpoint control problem formulated in (54), and is adapted from [57].

Theorem 2.1. *Let $\boldsymbol{u}^*$: $[t_0, t_f] \rightarrow \mathcal{U}$ be the optimal control input such that the corresponding state trajectory is $\boldsymbol{x}^*$: $[t_0, t_f] \rightarrow \mathbb{R}^n$. Then there exists a non-null function $\boldsymbol{J}_x^*$: $[t_0, t_f]$ and a constant $J_{x0}^* \leq 0$, such that:*

(1) $\boldsymbol{x}^*$ and $\boldsymbol{J}_x^*$ satisfy

$$\dot{\boldsymbol{x}}^{*T} = H_{\boldsymbol{J}_x}(t, \boldsymbol{x}^*, \boldsymbol{u}^*, \boldsymbol{J}_x^*, J_{x_0}^*) \tag{55}$$

$$\dot{\boldsymbol{J}}_x^{*T} = -H_{\boldsymbol{x}}(t, \boldsymbol{x}^*, \boldsymbol{u}^*, \boldsymbol{J}_x^*, J_{x_0}^*) \tag{56}$$

where the system Hamiltonian H is defined as

$$H(t, \boldsymbol{x}, \boldsymbol{u}, \boldsymbol{J}_x, J_{x_0}) = \boldsymbol{J}_x^T(t).f(t, \boldsymbol{x}, \boldsymbol{u}) + J_{x_0} L(t, \boldsymbol{x}, \boldsymbol{u}), \tag{57}$$

(2) $\forall t, t_0 \leq t \leq t_f$, the function H of variable $\boldsymbol{u}$ reaches its maximum when $\boldsymbol{u} = \boldsymbol{u}^*$, meaning

$$H(t, \boldsymbol{x}^*, \boldsymbol{u}^*, \boldsymbol{J}_x^*, J_{x0}^*) \geq H(t, \boldsymbol{x}^*, \boldsymbol{u}, \boldsymbol{J}_x^*, J_{x0}^*). \tag{58}$$

(3) If the final time t_f is set free, the following transversality equation is valid

$$H(t_f) = -\frac{\partial K(t_f, \boldsymbol{x}_f^*)}{\partial t}. \tag{59}$$

A proof of Theorem 2.1 is found in [57], chapter 4. Since $\mathcal{U} = \mathbb{R}^m$, the statement in (58) can be

translated into a necessary condition of optimality,

$$H_{\mathbf{u}} = 0. \tag{60}$$

The time derivative of the Hamiltonian can be written as,

$$\frac{dH}{dt} = \frac{\partial H}{\partial t} + H_{\mathbf{x}}.\frac{d\mathbf{x}}{dt} + H_{\mathbf{u}}.\frac{d\mathbf{u}}{dt} + H_{\mathbf{J}_x}.\frac{d\mathbf{J}_x}{dt}. \tag{61}$$

For an optimal input $\mathbf{u}^*$, and because of equations (55), and (60), the above expression reduces to

$$\frac{dH}{dt} = \frac{\partial H}{\partial t} + H_{\mathbf{x}}.H_{\mathbf{J}_x}^T + 0 - H_{\mathbf{J}_x}.H_{\mathbf{x}}^T = \frac{\partial H}{\partial t}, \tag{62}$$

which putting in words means that if the Hamiltonian does not depend explicitly on time, then is constant $\forall t, t_0 \leq t \leq t_f$. The following remark shall appear handy in the coming chapters of this thesis.

Remark 3. *If there are no penalties associated with final states, i.e. $K(t_f, \boldsymbol{x}_f) = 0$, and the final time is free, it is possible to see from the transversality condition (59) that $H(t_f) = 0$. Furthermore, if H does not depend explicitly on time, $H^* \equiv 0$ [57].*

Chapter 3

Optimal Trajectory Generation for a Quadrotor UAV on the Longitudinal Plane

This chapter presents an optimal real-time flight management algorithm for quadcopter UAVs in the sense of a trade-off between costs associated with body accelerations and total flight time while considering the system nonlinearities. This chapter is organized as follows. The optimal control problem formulation and the stated assumptions are presented in Section 3.1. Section 3.2 describes the proposed trajectory generation methodology using the Pontryagin's Minimum Principle (PMP). The drag effect is discussed in Section 3.3. Section 3.4 is dedicated to simulation results.

3.1 Problem Formulation

The objective of this chapter is to design trajectories for a quadrotor starting at a given position and arriving with zero speed at a target point (which can be the origin without loss of generality) by optimizing a trade-off of body accelerations and time of flight. In addition to the assumptions in section 2.1.2, the following is considered,

Assumption 3.1. *Yaw and roll angles are considered to be zero for longitudinal trajectories.*

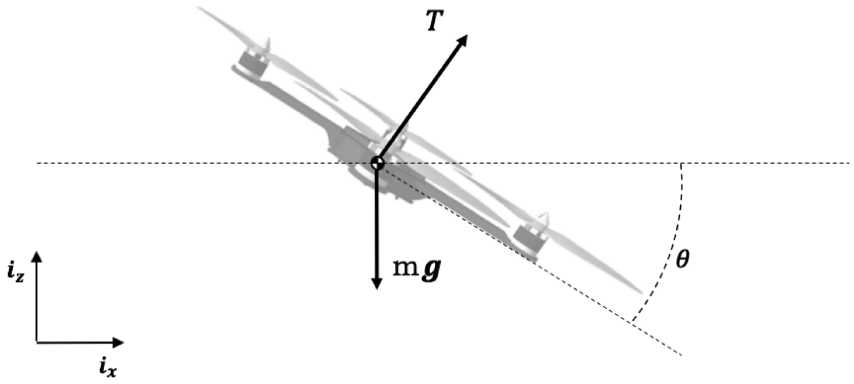

Figure 3.1: Quadrotor free body diagram and pitch angle convention.

The forces acting on the quadrotor are illustrated in Figure (3.1). The translational equations of motion in the x-z plane are

$$m\ddot{x} = Tsin(\theta), \quad m\ddot{z} = Tcos(\theta) - mg \tag{63}$$

where θ is the pitch angle, considered to be positive clockwise, g is the gravitational constant, T is the total propeller thrust, and m is the quadrotor mass. The influence of drag will only be studied in section 3.3.

Rewriting (63), considering horizontal and vertical accelerations as control inputs leads to

$$u_1 = \frac{T}{m}sin(\theta), \quad u_2 = \frac{T}{m}cos(\theta) - g, \tag{64}$$

respectively. The quadrotor's position is described by x and z and its velocity by v_x and v_z. Position and velocities form the state vector $\mathbf{x} = [x \;\; z \;\; v_x \;\; v_z]^T$.

The optimal control problem for trajectory generation can be stated as

$$\min_{\mathbf{u},t_f} \int_0^{t_f} \left(\frac{1}{2}\mathbf{u}^T\mathbf{u} + C_I\right) d\tau \tag{65}$$

$$subject\ to\ (63),\ \mathbf{x}(0) = \mathbf{x_0},\ \mathbf{x}(t_f) = \mathbf{x_f} \tag{66}$$

with $\mathbf{x_0}^T = [x_0\ z_0\ v_{x_0}\ v_{z_0}]$, $\mathbf{x_f}^T = [0\ 0\ 0\ 0]$, $\mathbf{u}^T = [u_1\ u_2]$, and C_I is the trade-off coefficient between

costs associated with body acceleration and total flight time. Note that the cost index (C_I) unit is m^2/s^4. The higher the value of C_I the higher is the weight on the total flight time (t_f).

3.2 Problem Solution

Theorem 3.1. *Assume that $C_I > 0$ is given. Then the solution to the optimal control problem (65)-(66) is*

$$\theta^* = \begin{cases} tan^{-1}\left(\frac{u_1^*}{u_2^*+g}\right), & u_2^* \neq -g \\ \pi/2, & u_2^* = -g, u_1^* > 0 \\ -\pi/2, & u_2^* = -g, u_1^* < 0 \end{cases}$$
$$T^* = \begin{cases} \frac{m(u_2^*+g)}{cos(\theta^*)}, & \theta^* \neq \pm\pi/2 \\ m\, u_1^*, & \theta^* = \pi/2 \\ -m\, u_1^*, & \theta^* = -\pi/2 \end{cases} \tag{67}$$

with $\theta^* \in [-\pi/2, \pi/2]$, where

$$\begin{bmatrix} u_1^{*2} \\ u_2^{*2} \end{bmatrix} = \begin{bmatrix} 2(C_I + J_x v_x + J_z v_{z_0}) - J_{v_z(0)}{}^2 \\ 2(C_I + J_z v_z + J_x v_{x_0}) - J_{v_x(0)}{}^2 \end{bmatrix} \tag{68}$$

and the costate variables are given by

$$J_x = \frac{6(2x_0 + v_{x_0} t_f)}{t_f^3},\ J_z = \frac{6(2z_0 + v_{z_0} t_f)}{t_f^3}, \tag{69}$$

$$J_{v_x}(0) = \frac{2(3x_0 + 2v_{x_0} t_f)}{t_f^2},\ J_{v_z}(0) = \frac{2(3z_0 + 2v_{z_0} t_f)}{t_f^2}. \tag{70}$$

Proof. Let the cost-to-go be defined as

$$J = \int_0^{t_f} \left(\frac{1}{2}\mathbf{u}^T\mathbf{u} + C_I\right) d\tau \tag{71}$$

The Hamiltonian of the system is

$$H = \frac{1}{2}u_1^2 + \frac{1}{2}u_2^2 + C_I + J_x v_x + J_{v_x} u_1 + J_z v_z + J_{v_z} u_2 \tag{72}$$

A necessary condition for optimality is $H_{u_1} = H_{u_2} = 0$ (where H_u is the partial derivative of H with respect to u) which yields

$$u_1^* = -J_{v_x}, \;\; u_2^* = -J_{v_z}. \tag{73}$$

Therefore, from the dynamics (64) we have

$$J_{v_x} = -\dot{v}_x, \;\; J_{v_z} = -\dot{v}_z \tag{74}$$

From the Hessian matrix of H with respect to u_1 and u_2 we get the Legendre-Clebsch sufficient condition of optimality

$$\begin{bmatrix} H_{u_1 u_1} & H_{u_1 u_2} \\ H_{u_2 u_1} & H_{u_2 u_2} \end{bmatrix} = \begin{bmatrix} 1 & 0 \\ 0 & 1 \end{bmatrix} > 0. \tag{75}$$

As in remark 3, there are no penalties associated with final states in our cost functional. Therefore according to the transversality equations $H(t_f) = 0$. Additionally, the final time is considered to be free, and the Hamiltonian does not depend explicitly on time, which together with $H(t_f) = 0$ makes $\dot{H}(t) = 0$ and $H^* \equiv 0$ [57]. Replacing u_1^* and u_2^* from (73) in the system's Hamiltonian (72) results in

$$J_{v_x}^2 + J_{v_z}^2 = 2(C_I + J_x v_x + J_z v_z) \tag{76}$$

According to PMP and Hamilton's equations [58], [57],

$$\begin{bmatrix} \dot{J}_x \\ \dot{J}_{v_x} \\ \dot{J}_z \\ \dot{J}_{v_z} \end{bmatrix} = \begin{bmatrix} 0 \\ -J_x \\ 0 \\ -J_z \end{bmatrix} \tag{77}$$

Consequently, J_x and J_z are constant in time and J_{v_x} and J_{v_z} are linear functions that can be written

in the form

$$J_{v_x}(t) = -J_x t + J_{v_x}(0) \tag{78}$$

$$J_{v_z}(t) = -J_z t + J_{v_z}(0) \tag{79}$$

Having (78), and (79), one can integrate (74) to find expressions for $v_x(t)$ and $v_z(t)$.

$$v_x(t) = -\int_0^t J_{v_x}(\tau)d\tau + v_x(0) = \frac{J_x t^2}{2} - J_{v_x}(0)t + v_x(0) \tag{80}$$

$$v_z(t) = -\int_0^t J_{v_z}(\tau)d\tau + v_z(0) = \frac{J_z t^2}{2} - J_{v_z}(0)t + v_z(0) \tag{81}$$

Integrating (80) yields

$$x(t) = \int_0^t v_x(\tau)d\tau + x(0) = \frac{J_x t^3}{6} - \frac{J_{v_x}(0)t^2}{2} + v_{x_0}t + x(0) \tag{82}$$

$$z(t) = \int_0^t v_z(\tau)d\tau + z(0) = \frac{J_z t^3}{6} - \frac{J_{v_z}(0)t^2}{2} + v_{z_0}t + z(0) \tag{83}$$

It is possible to replace the expressions (78), and (79) and (80) into the system Hamiltonian equation described in (76) to obtain

$${J_{v_x}}^2 = 2(C_I + J_x v_x + J_z v_{z_0}) - J_{v_z}^2(0). \tag{84}$$

Using (73) and (76), equation (84) reduces to

$$u_1^* = \pm\sqrt{2(C_I + J_x v_x + J_z v_{z_0}) - {J_{v_z(0)}}^2} \tag{85}$$

and u_2^* is obtained similarly as

$$u_2^* = \pm\sqrt{2(C_I + J_z v_z + J_x v_{x_0}) - {J_{v_x(0)}}^2} \tag{86}$$

The system of equation formed by (76), (80), (81), (82), and (83) at the final time can be solved for the unknowns J_x, J_z, $J_{v_x}(0)$, $J_{v_z}(0)$, and t_f. Doing this, the final time is a real positive root of

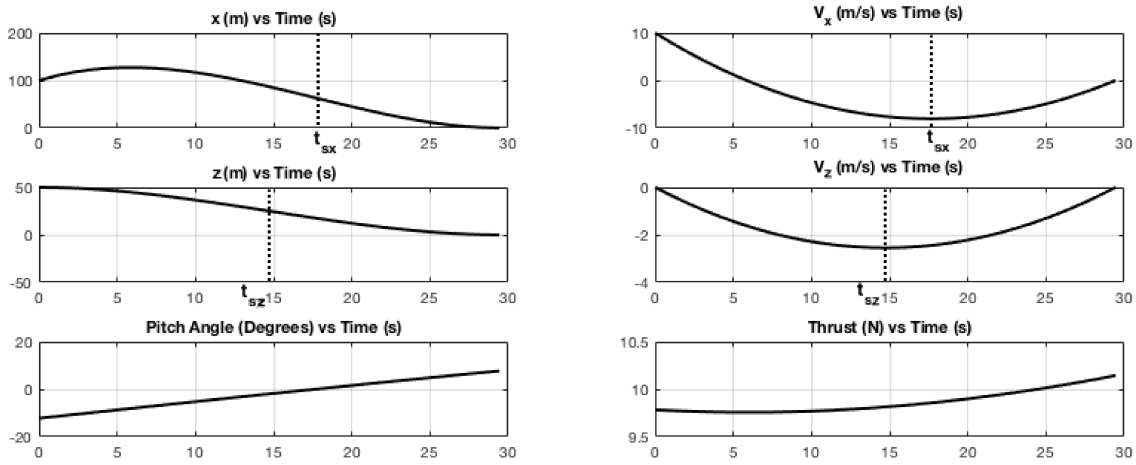

Figure 3.2: Optimal trajectories.

the following quartic polynomial $P(Z)$,

$$C_I Z^4 - 2(v_{x_0}^2 + v_{z_0}^2)Z^2 - 12(v_{x_0}x_0 + v_{z_0}z_0)Z - 18(x_0^2 + z_0^2) = 0 \tag{87}$$

In this case, because the zero and second order terms are negative, there are at least two real roots and according to the Descartes' rule of signs one of those roots is positive. The remaining unknowns for the general solution can then be obtained by the roots of the fourth order linear system composed by (80), (81), (82), and (83) at the final time, which yields (69), and (70). The results can be replaced back into equations (80), (81), (82), and (83) in order to get expressions for $x(t)$, $z(t)$, $v_x(t)$, and $v_z(t)$. Finally, the thrust profile and pitch angle can then be obtained by inverting the change of input coordinates in equations (64), which finishes the proof. □

Remark 4. *Given a specific C_I, it is possible to determine the optimal inputs u_1^* and u_2^* knowing the velocity states (v_x, v_z) and initial conditions (x_0, z_0, v_{x_0}, v_{z_0}).*

Remark 5. *For the special case in which the quadrotor is initially at zero speed ($v_{x_0} = 0$ and $v_{z_0} = 0$) the final time is*

$$t_f = \left(\frac{18(x_0^2 + z_0^2)}{C_I}\right)^{\frac{1}{4}} \tag{88}$$

Corollary 3.1.1. *Assume $x_0 > 0$ and $z_0 > 0$, then the optimal control law that achieves the state*

(0, 0, 0, 0) is given by the state feedback form

$$u_1^* = \begin{cases} -\sqrt{2J_x(v_x - v_{x_0}) + J_{v_x}^2(0) - 2J_z v_{z_0}}, & t < t_{s_x} \\ 0 & , \ t = t_{s_x} \\ +\sqrt{2J_x(v_x - v_{x_0}) + J_{v_x}^2(0) - 2J_z v_{z_0}}, & t > t_{s_x} \end{cases}$$
$$u_2^* = \begin{cases} -\sqrt{2J_z(v_z - v_{z_0}) + J_{v_z}^2(0) - 2J_x v_{x_0}}, & t < t_{s_z} \\ 0 & , \ t = t_{s_z} \\ +\sqrt{2J_z(v_z - v_{z_0}) + J_{v_z}^2(0) - 2J_x v_{x_0}}, & t > t_{s_y} \end{cases} \tag{89}$$

where the switching times occur at

$$t_{s_x} = \frac{(3x_0 + 2v_{x_0}t_f)t_f}{6x_0 + 3v_{x_0}t_f}, \ t_{s_z} = \frac{(3z_0 + 2v_{z_0}t_f)t_f}{6z_0 + 3v_{z_0}t_f} \tag{90}$$

Proof. The switching time of u_1^* occurs when the acceleration along x axis is zero, meaning from equation (74) that $J_{v_x}(t_{s_x}) = 0$, or similarly, from equation (78), and (79), that

$$t_{s_x} = J_{v_x}(0)/J_x. \tag{91}$$

Equations (69), and (70) can then be replaced into (91) which yields (90). Repeating this procedure for z finishes the proof. □

Remark 6. *If the quadrotor is initially at zero speed, the switching time of each coordinate is equal to half of final time.*

Remark 7. *Since the pitch angle was considered as an input, it is important to note that the generated optimal trajectories allow pitch discontinuities. However, this simplification has a shallow impact on the overall performance since the solution is interpreted as a trajectory reference for the trajectory tracking controller that will then smooth out the dynamic response in closed-loop.*

3.3 Influence of Drag

UAVs are capable of reaching certain speeds in which drag forces start to contribute significantly to the dynamics [50], [51]. This section will address the case when drag cannot be neglected. Specifically, this section addresses the cases where the distances to be covered in the horizontal direction are much greater than in the vertical direction, as discussed in section 2.1.4. The following assumption is added.

Assumption 3.2. *The translational drag force in a quadrotor is modelled linearly as* $D_x = k_d\dot{x}$.

Under the assumptions (3.1-3.2) and equation (9), one can obtain the following translational dynamics

$$m\ddot{x} = Tsin(\theta) - k_d\dot{x}, \quad m\ddot{z} = Tcos(\theta) - mg. \tag{92}$$

The original optimal control problem can then be restated as

$$\min_{\mathbf{u},t_f} \int_0^{t_f} \left(\frac{1}{2}\mathbf{u}^T\mathbf{u} + C_I\right) d\tau \tag{93}$$

$$subject\ to \quad \dot{\mathbf{x}} = \mathbf{f}(\mathbf{x},\mathbf{u}) \tag{94}$$

$$\mathbf{x}(0) = \mathbf{x_0},\ \mathbf{x}(t_f) = \mathbf{x_f} \tag{95}$$

with $\mathbf{x_0}^T = [x_0\ z_0\ 0\ 0], \mathbf{x_f}^T = [0\ 0\ 0\ 0], \mathbf{u}^T = [u_1\ u_2]$, and

$$\mathbf{f}(\mathbf{x},\mathbf{u}) = \begin{bmatrix} v_x \\ v_z \\ u_1 - kv_x \\ u_2 \end{bmatrix}$$

where the definition of u_1 and u_2 is given by the equations (64), and $k = k_d/m > 0$.

Theorem 3.2. *Assume that the quadrotor never turns off its propellers, and a positive trade-off coefficient* C_I *is given. Finding the quadrotor optimal pitch angle and thrust profiles which minimize*

the cost functional described by (93)-(95) is equivalent to solving the set of equations

$$\begin{cases} J_z = 12z_0/t_f^3 \\ J_{v_z}(0) = 6z_0/t_f^2 \\ J_x = k^3 x_o sinh(kt_f)/\Delta \\ J_{v_x}(0) = k^2 x_o(cosh(kt_f) - 1)/\Delta \\ J_{v_x}^2(t_f) + J_{v_z}^2(t_f) = 2C_I \end{cases} \tag{96}$$

where

$$\Delta = kt_f sinh(kt_f) - 2cosh(kt_f) + 2 \neq 0 \tag{97}$$

and finally, applying the identities (67) .

Proof. The dynamics in (92) and cost functional in (93) yield the following Hamiltonian.

$$H = \frac{1}{2}u_1^2 + \frac{1}{2}u_2^2 + C_I + J_x v_x + J_{v_x}(u_1 - kv_x) + J_z v_z + J_{v_z} u_2 \tag{98}$$

The necessary and sufficient conditions of optimality from the previous section remain unchanged, i.e.,

$$u_1^* = -J_{v_x}, \;\; u_2^* = -J_{v_z}, \tag{99}$$

and,

$$\begin{bmatrix} H_{u_1u_1} & H_{u_1u_2} \\ H_{u_2u_1} & H_{u_2u_2} \end{bmatrix} = \begin{bmatrix} 1 & 0 \\ 0 & 1 \end{bmatrix} > 0. \tag{100}$$

The PMP and Hamilton's equations become

$$\begin{bmatrix} \dot{J}_x \\ \dot{J}_{v_x} \\ \dot{J}_z \\ \dot{J}_{v_z} \end{bmatrix} = \begin{bmatrix} 0 \\ -J_x + kJ_{v_x} \\ 0 \\ -J_z \end{bmatrix}. \tag{101}$$

As one can expect, the z coordinate kinematic equations from last section remain the same. However, the x coordinate kinematic equations are derived as follows. Because J_x is constant J_{v_x} can be written as

$$J_{v_x}(t) = \left(J_{v_x}(0) - \frac{J_x}{k}\right)e^{kt} + \frac{J_x}{k}. \tag{102}$$

Having J_{v_x} expressed in (102), one can obtain $v_x(t)$ by integrating $\dot{v}_x = u_1 - kv_x$, which from (99) becomes

$$\dot{v}_x = -J_{v_x} - kv_x. \tag{103}$$

Considering the initial condition $v_x(0) = 0$, the integration yields the following,

$$v_x(t) = \frac{J_x}{k^2}(cosh(kt) - 1) - \frac{J_{v_x}(0)}{k}sinh(kt). \tag{104}$$

Finally, $x(t)$ is found by integrating (104) as

$$x(t) = x_0 + \frac{J_x}{k^3}(sinh(kt) - kt) - \frac{J_{v_x}(0)}{k^2}(cosh(kt) - 1) \tag{105}$$

It is shown in Appendix A.1 that expressions (104) and (105) reduce respectively to expressions (80) and (82) of the previous section when the drag coefficient k approaches zero, as expected.

The kinematic and dynamic equations (104), (105), (81), and (83) form a similar system of equations that can be solved at the final time. This procedures yields,

$$J_x = \frac{k^3 x_o sinh(kt_f)}{\Delta}, \quad J_{v_x}(0) = \frac{k^2 x_o(cosh(kt_f) - 1)}{\Delta}, \tag{106}$$

$$J_z = \frac{12z_0}{t_f^3}, \quad J_{v_z}(0) = \frac{6z_0}{t_f^2}, \tag{107}$$

with, $\Delta = kt_f sinh(kt_f) - 2cosh(kt_f) + 2 \neq 0$.

As in remark 3, because there are no penalties associated with final states in our cost functional, $H(t_f) = 0$. Additionally, the final time is set to be free, and the Hamiltonian does not depend explicitly on time, which together with $H(t_f) = 0$ makes $H^* \equiv 0$. Then, from the Hamiltonian and

the expressions in (99),

$$H = \frac{1}{2}(-J_{v_x})^2 + \frac{1}{2}(-J_{v_z})^2 + C_I + J_x v_x + J_{v_x}((-J_{v_x}) - k v_x) + J_z v_z + J_{v_z}(-J_{v_z}) = 0. \quad (108)$$

At the final time $v_x = 0$, and $v_z = 0$, which results in

$$J_{v_x}^2(t_f) + J_{v_z}^2(t_f) = 2C_I. \quad (109)$$

The expression (109) composes the fifth equation needed in the system of equations of this theorem. Similarly, the optimal control law is finally obtained from (99), which completes the proof. □

3.4 Simulation Results

Table 3.1: Hummingbird quadrotor parameters

Mass m	0.71 kg
Propeller size d	20,32 cm
LiPo battery capacity Q_o	2100 mAh
Battery voltage $U_{nominal}$	11.1 V
Max Thrust	20 N
Endurance	up to 15 min
Max motor power	4 x 80 W

This section presents the results of simulations for the solution discussed in the previous sections. The Ascending Technologies AscTec Hummingbird (see Figure 3.3) quadrotor parameters were adopted according to table 3.1, obtained from [59].

3.4.1 Optimal Trajectories

Figure 3.2 shows the resulting trajectories for position, velocity, pitch angle and thrust. For simulation purposes the quadrotor's initial state is considered to be $(x_0, z_0, v_{x_0}, v_{z_0}) = (100, 50, 10, 0)$, the trade-off coefficient (C_I) is set to 1, and no drag is considered. The final time obtained in the simulation was 29.45 seconds. Because $v_{z_0} = 0\, m/s$, the switching time for the coordinate y occurs exactly at the half point of flight time. On the other hand, because $v_{x_0} = -10\, m/s$ the switching

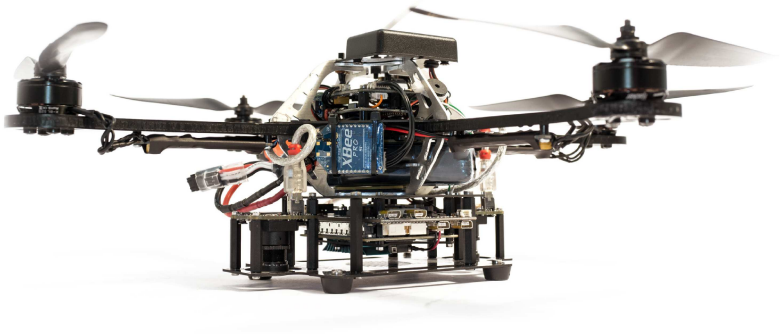

Figure 3.3: Asctec Hummingbird quadrotor

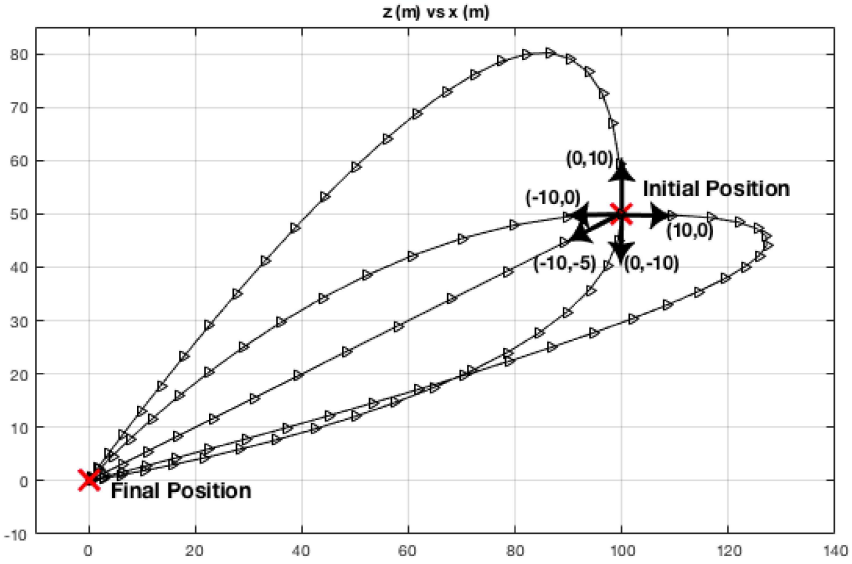

Figure 3.4: Optimal Paths.

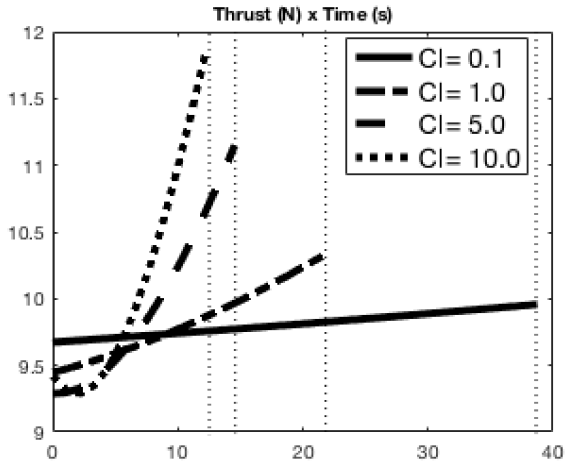

Figure 3.5: Thrust Profile for different Cost Indices.

time for the coordinate x occurs later at t = 17.64 seconds. Similarly, the anti-symmetry of the pitch angle with respect to $t = t_f/2$ axis does not occur because $v_{x_0} \neq 0\ m/s$. Additionally, the symmetry of the thrust profile with respect to $t = t_f/2$ axis would occur when $v_{x_0} = 0\ m/s$, $v_{z_0} = 0\ m/s$, and the ratio between x_0 and z_0 is equal to 1. As predicted, the resulted pitch angle profile contains discontinuities at initial and final states, but shall have a low impact on long-distance flights performance, since trajectory tracking flight controllers are able to stabilize the desired attitude very quickly in the case of multirotors.

Figure 3.4 illustrates optimal trajectories for quadrotors starting at the same position but with different initial velocities. The interval between two consecutive marks represents 1 second. The initial velocity vectors are represented by arrows. As expected, trajectories in which the initial velocities are unfavorable to move in the direction of the final target take longer than the trajectories with favorable initial conditions. The optimal path becomes a straight line if the initial velocity vector $\boldsymbol{v_0} = (v_{x_0}, v_{z_0})$ can be written as $\boldsymbol{v_0} = c_0\boldsymbol{x_0}$ where c_0 is a real scalar and $\boldsymbol{x_0}$ is the initial position vector.

Because the controller law is obtained analytically (closed-form expression), real-time path generation or replanning would not require high onboard processing capabilities.

3.4.2 Trade-off Coefficient

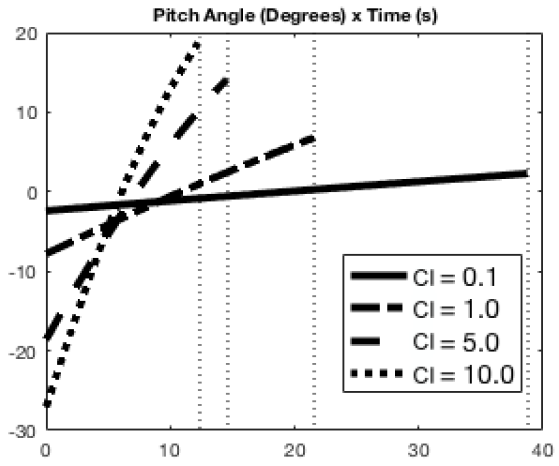

Figure 3.6: Pitch Angle for different Cost Indices.

C_I is the tuning parameter of the solution, which is used to address the control energy and final time trade-off. Figure 3.5 shows the influence of C_I on the thrust profile in the case where $(x_0, z_0, v_{x_0}, v_{z_0}) = (100, 50, 0, 0)$. As expected, higher cost indices provide shorter flight times but require a higher thrust. Similarly, the behavior of the pitch angle is simulated in figure 3.6 considering the same initial conditions. Higher cost indices require more aggressive maneuvers (larger pitch angles).

The Pareto-optimal trade-off curve between the total flight time and the amount of control energy required for different values of C_I is shown in figure 3.7. From this plot, it is possible to conclude that if the cost index increases the total flight time decreases and the control energy consumed increases.

3.4.3 Influence of Drag

Figure 3.8 shows the influence of drag in the optimal horizontal trajectory. The initial state is $(x_0, z_0, v_{x_0}, v_{z_0}) = (1000, 10, 0, 0)$ and C_I is set to 1. Curves are plotted for situations where the drag coefficient ($k = k_d/m$) varies from 0.05 to 0.20. Intuitively, higher drag coefficients imply longer flight times. The drag effect also produces a limitation on the maximum magnitude of speed. Requiring additional energy for accomplishing the goal, the drag effect demands that the system operate at extremum pitch angle and thrust for longer.

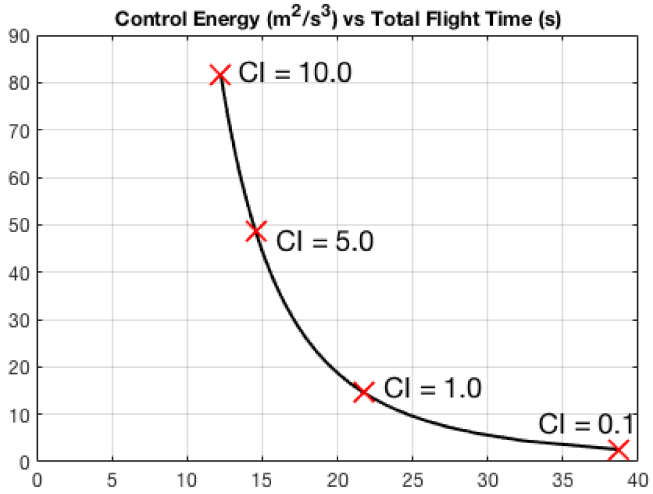

Figure 3.7: Pareto-optimal trade-off curve.

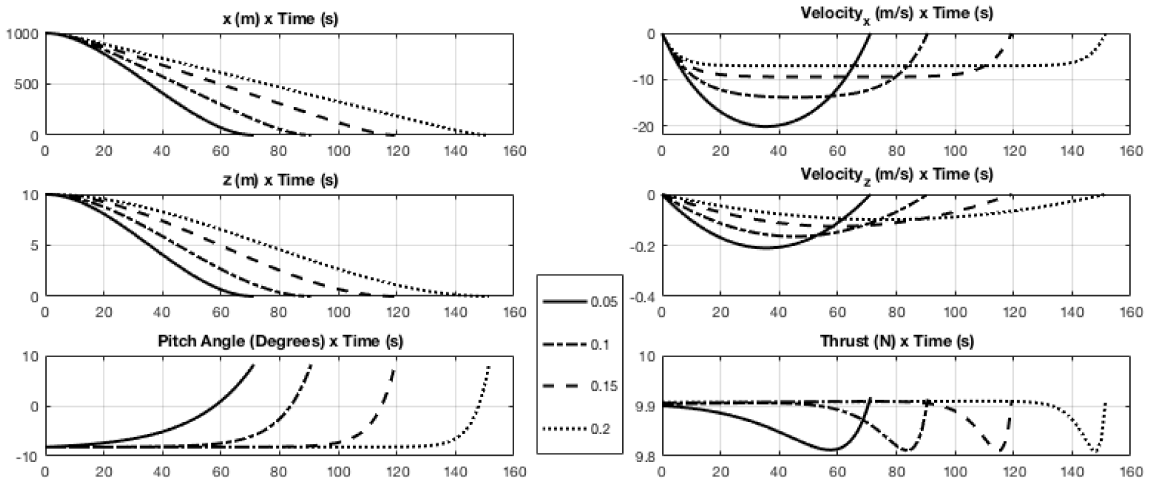

Figure 3.8: Optimal trajectories - Different drag coeficients.

Chapter 4

Constant Altitude Steady Forward Flight Economy Mode for a Quadcopter UAV

When flying long trajectories, UAVs tend to remain most of the time in the steady state situation. This chapter aims at saving battery discharge by presenting an optimal flight management formulation for quadcopter UAVs in the sense of a trade-off between costs associated with battery consumption and total flight time for the steady forward flight at constant altitude. The proposed formulation considers the saturation of the system input. This chapter is organized as follows. Assumptions are stated in Section 4.1. The optimal control problem formulation for the economy mode and maximum range flights are presented in Sections 4.2 and 4.3. Section 4.4 is dedicated to simulations.

4.1 Assumptions

This section studies the situation of a quadrotor performing a steady forward flight maneuver at a constant speed or, similarly to the term used for commercial airplanes, *in cruise* at a constant altitude. In order to formulate an energy-efficient framework for the trajectory planning problem of a UAV, the following assumptions are added to the ones in Section 2.1.2.

Assumption 4.1. *Roll and yaw angles are considered to be zero for forward flight.*

Assumption 4.2. *The forward speed (v_x) is assumed to be constant, which describes a steady forward flight with constant pitch angle.*

Assumption 4.3. *The quadcopter is considered to remain at the same altitude.*

Assumption 4.4. *The efficiency of the electromechanical conversion (η) is considered to be constant.*

Assumption 4.5. *The quadrotor flies at velocities in which the power due the parasitic drag is small compared with the other components of power.*

Assumption 4.6. *The rotors operate in a range of angular velocities in which the ratio $\frac{C_M}{{C_T}^{3/2}}$ is assumed to be constant. This assumption is equivalent to consider a constant rotor figure of merit (FM).*

Assumption 4.7. *Tip losses, wake swirl, and non-uniform inflow are minor contributors, and are neglected in the power consumption model.*

Assumption 4.8. *The adopted model for the drag effect has a linear term in the speed and a quadratic term in the speed as derived in Section 2.1.4, $D_x = k_1 v_x + k_2 {v_x}^2$, where the positive drag coefficients k_1 and k_2, experimentally obtained, contain the dependency on the medium, body dimensions, geometry, and orientation.*

Assumption 4.9. *The battery is considered to operate in the nominal zone, i.e., the region where the voltage output does not vary significantly with the State of Charge (SOC) as discussed in Section 2.1.5.*

4.1.1 Power Consumption

Currently, the literature about the power consumption of electrical powered UAVs is not vast. Equations used in this section come from the theory developed for helicopters in textbooks [60] and [61]. There are three main components of power in rotorcraft vehicles: profile power (P_o), induced power (P_{ind}), and parasite power (P_p). Profile power is the portion of power necessary to overcome

the rotor aerodynamic drag force. Induced power is the component of power required to induce airflow through the rotor disk. Finally, parasite power is spent due to the parasitic drag, i.e., the power spent in the friction caused by the motion of the UAV through the air. The term total power P_{total} will be used to indicate the sum of the three components.

From momentum theory (see Subsection 2.1.3), equation (22) gives the magnitude of the induced air velocity in hover condition

$$v_h^2 = \frac{T}{2\rho A}, \tag{110}$$

therefore, from equation (16), the power generating thrust in one single propeller in hovering is

$$P_{thrust} = T v_h = T\sqrt{\frac{T}{2\rho A}}, \tag{111}$$

which is a well known expression. The same procedure can be made for the forward flight condition, where the actual wind velocity is

$$\mathbf{v}_1 = -v_x \mathbf{i_x} + v_{ind}\mathbf{b'_z}, \tag{112}$$

then term,

$$\mathbf{v}_1.\mathbf{b'_z} = v_x \sin\theta + v_{ind}, \tag{113}$$

where θ is the pitch angle depicted in Figure 4.1. From equation (16), the power generating thrust in the forward flight, i.e., is,

$$P_{thrust} = P_{ind} + P_p = T(v_{ind} + v_x \sin\theta), \tag{114}$$

in this sense, the first and second terms in P_{thrust} represent the induced and parasite components of power. From (20),

$$T = 2\rho A|\mathbf{v}_1|\mathbf{v}_{ind}.\mathbf{b'_z} = 2\rho A\sqrt{(v_x\cos\theta)^2 + (v_{ind} + v_x\sin\theta)^2}v_{ind}, \tag{115}$$

which yields,

$$v_{ind} = \frac{T}{2\rho A\sqrt{(v_x\cos\theta)^2 + (v_{ind} + v_x\sin\theta)^2}}. \tag{116}$$

Replacing term $(v_{ind} + v_x \sin\theta)$ of (116) back in (114), yields,

$$P_{thrust} = P_{ind} + P_p = T\sqrt{\frac{T^2}{4\rho^2 A^2 v_{ind}^2} - v_x^2 \cos^2\theta}. \tag{117}$$

As expected, (110) is recovered when $v_x = 0$, since $v_{ind} = v_h$ in this case. Therefore, the approximation $v_{ind} \approx v_h$ leads to,

$$P_{thrust} = P_{ind} + P_p \approx T\sqrt{\frac{T}{2\rho A}}. \tag{118}$$

The profile power can be estimated using the blade element theory (see Subsection 2.1.3). The power into a single propeller is

$$P_o = \Omega M. \tag{119}$$

where Ω is the propeller angular speed and M is the rotor torque. Replacing (37) into (119) yields,

$$P_o \approx C_M \Omega^3 \tag{120}$$

Equation (36) can then be solved for Ω and plugged into (120), which results in

$$P_o \approx \frac{C_M T^{3/2}}{C_T^{3/2}}. \tag{121}$$

Note that equations (36) and (37), were derived under the Assumption 2.8, under circumstances which are equivalent to the ones in Assumption 4.5.

The total power delivered to the rotor is then

$$P_{total} = P_{ind} + P_p + P_o = P_{thrust} + P_o \approx T\sqrt{\frac{T^2}{4\rho^2 A^2 v_{ind}^2} - v_x^2 \cos^2\theta} + \frac{C_M T^{3/2}}{C_T^{3/2}}. \tag{122}$$

Under Assumption 4.5, (122) becomes

$$P_{total} \approx T\sqrt{\frac{T}{2\rho A}} + \frac{C_M T^{3/2}}{C_T^{3/2}} \;\alpha\, T^{3/2}. \tag{123}$$

This consumption model suits well the flight conditions studied in this thesis. For a more complete

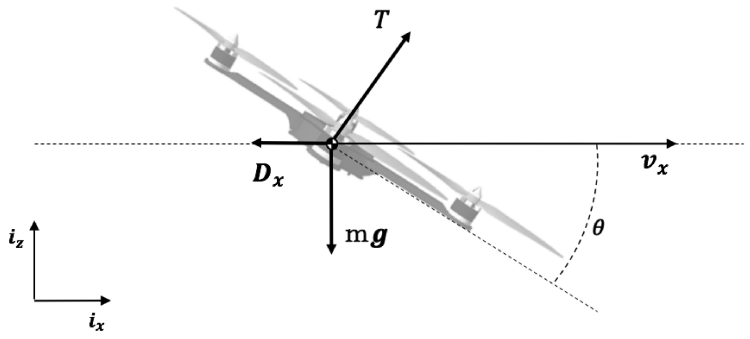

Figure 4.1: Quadrotor free body diagram

model the reader is referred to [62].

4.1.2 Energy Conversion

Equation (123) was derived for one propeller. The total power delivered to the four propellers is

$$P_R = \zeta \sum_{i=1}^{4} {T_i}^{3/2} \tag{124}$$

where $\zeta = \frac{1}{\sqrt{2\rho A}} + \frac{C_M}{C_T^{3/2}} > 0$. Under the assumptions stated in Subsection 2.1.5, the power delivered to the four propellers is considered to be equal to the power provided by the battery P_e times the overall efficiency of the electromechanical conversion η ($0 < \eta < 1$).

$$P_e \eta = -U\dot{q}\eta = \zeta \sum_{i=1}^{4} {T_i}^{3/2} \tag{125}$$

where U and q are the battery voltage and charge, respectively. From assumption 4.9 the voltage is considered constant ($U = U_{nominal}$).

From assumptions 4.1 and 4.2, each propeller provides the same amount of thrust ($T_i = T/4$, $i = 1, ..., 4$). Consequently, the identity

$$\sum_{i=1}^{4} {T_i}^{3/2} = \frac{1}{2} T^{3/2} \tag{126}$$

holds.

4.1.3 Constant Altitude and Steady Forward Flight Model

Under assumptions 4.1 to 4.3, the equations in (9) are reduced to

$$\dot{x} = v_x, \tag{127}$$

$$\dot{v_x} = \frac{T(\theta)sin(\theta)}{m} - \frac{k_1 v_x + k_2 {v_x}^2}{m} = 0, \tag{128}$$

$$\dot{z} = v_z = 0, \tag{129}$$

$$\dot{v_z} = -g + \frac{T(\theta)cos(\theta)}{m} = 0, \tag{130}$$

with $\theta \in (0, \pi/2)$ (see Figure 4.1), and $T(\theta) = \frac{mg}{cos(\theta)}$ due to equation (130).

Equation (128) is quadratic in $\dot{x}$, with solutions,

$$v_x = \frac{-k_1 \pm \sqrt{{k_1}^2 + 4k_2 T(\theta)sin(\theta)}}{2k_2}. \tag{131}$$

Since $k_1 > 0$, $k_2 > 0$, and $T(\theta)sin(\theta) > 0$, equation (131) has one positive and one negative root. Since a negative root is not a possible solution for the steady forward flight situation,

$$v_x = F(\theta) = \frac{-k_1 + \sqrt{{k_1}^2 + 4k_2 T(\theta)sin(\theta)}}{2k_2}. \tag{132}$$

From (125), (127), (128), and (132) one can write the complete system dynamics in the following form

$$\begin{aligned} \dot{x} &= F(T(\theta)), \\ \ddot{x} &= 0, \\ \dot{q} &= -\frac{\zeta T(\theta)^{3/2}}{2\eta U}. \end{aligned} \tag{133}$$

4.2 Economy Mode Optimal Control Problem

In this section an Optimal Control Problem (OCP) for the longitudinal flight of a quadcopter is formulated. The objective is to minimize the Operating Cost (OC) composed of a time-related cost

(\$/s) $C_t \geq 0$ and the cost of the battery charge (\$/C) $Cq > 0$,

$$OC = \int_0^{t_f} (C_t + C_q|\dot{q}|)d\tau \tag{134}$$

Using (130), minimizing OC is equivalent to minimizing the following cost function,

$$J = \int_0^{t_f} (C_I + T^{3/2})d\tau = \int_0^{t_f} \left(C_I + \left(\frac{mg}{cos(\theta)}\right)^{3/2}\right)d\tau \tag{135}$$

where $C_I = \frac{2C_t\eta U}{C_q\zeta} > 0$ encapsulates the trade-off parameter (C_t/C_q) and the other constants of the problem. Note that in this case, differently form the previous chapter, the cost index (C_I) is expressed in $N^{3/2}$. Intuitively, higher cost indices penalize more the flight time but require a faster battery discharge. Furthermore, the minimum energy consumption case is achieved when the cost index is set to zero.

Without loss of generality, the quadcopter is considered to start at $t_0 = 0$ at the origin, and arrive at the final position x_f at $t = t_f$. The maximum allowed pitch angle must verify the constraint

$$\theta_{max} = arccos\left(\frac{mg}{T_{max}}\right) < \pi/2 \tag{136}$$

where T_{max} is the maximum allowed thrust. For a steady forward flight at constant altitude, the minimum energy OCP can then be stated as

$$\begin{aligned} J^* = \min_{\theta, t_f} \int_0^{t_f} G(\theta)d\tau \\ s.t. \\ v_x = F(\theta) = \frac{-k_1 + \sqrt{{k_1}^2 + 4k_2\, m\, g\, tan(\theta)}}{2k_2}, \\ \dot{v_x} = 0, \\ x(0) = 0, x(t_f) = x_f > 0, \\ 0 < \theta \leq \theta_{max} \end{aligned} \tag{137}$$

where $G(\theta) = C_I + \left(\frac{mg}{cos(\theta)}\right)^{3/2}$ and the final time t_f is free.

4.2.1 Minimum-energy problem

Then following OCP can then be stated,

$$\begin{aligned} J^* = \min_{v_x, t_f} \int_0^{t_f} \left(CI + ((k_1 v_x + k_2 v_x^2)^2 + (mg)^2)^{3/4} \right) d\tau \\ s.t. \\ \dot{x} = v_x, \\ \dot{v_x} = 0, \\ x(0) = 0, x(t_f) = x_f > 0, \\ 0 < v_x \leq \frac{-k_1 + \sqrt{{k_1}^2 + 4k_2\ m\ g\ tan(\theta_{max})}}{2k_2} \end{aligned} \tag{138}$$

Proposition 4.1. *The OCP stated in (138) is equivalent to (137)*

Proof. From equations (128) and (130), it is possible to obtain the following identities,

$$\begin{aligned} T(\theta) sin\theta = k_1 v_x + k_2 v_x^2, \\ T(\theta) cos\theta = mg. \end{aligned} \tag{139}$$

Therefore,

$$T(\theta) = \sqrt{(k_1 v_x + k_2 v_x^2)^2 + (mg)^2}, \tag{140}$$

where the negative root was omitted since $T > 0$. The ratio of equations in (139) also gives

$$\theta = tan^{-1}\left(\frac{k_1 v_x + k_2 v_x^2}{mg}\right), \tag{141}$$

and

$$T(\theta) sin\theta = mg\ tan\theta. \tag{142}$$

Identity (140) can be replaced into the dynamics (133), which yields the following dynamics,

$$\begin{aligned} \dot{x} = v_x = F(T(\theta)) = \frac{-k_1 + \sqrt{{k_1}^2 + 4k_2 T(\theta) sin(\theta)}}{2k_2}, \\ \dot{v_x} = 0, \\ \dot{q} = -\frac{\zeta T(\theta)^{3/2}}{2\eta U} = -\frac{\zeta((k_1 v_x + k_2 v_x^2)^2 + (mg)^2)^{3/4}}{2\eta U}. \end{aligned} \tag{143}$$

Then, defining v_x as the control input, the cost functional (137) can be rewritten as

$$J^* = \min_{v_x, t_f} \int_0^{t_f} \left(CI + ((k_1 v_x + k_2 v_x^2)^2 + (mg)^2)^{3/4} \right) d\tau. \tag{144}$$

Finally, from (142),

$$F(\theta) = \frac{-k_1 + \sqrt{{k_1}^2 + 4k_2\ m\ g\ tan(\theta)}}{2k_2}, \tag{145}$$

which is monotonic in the studied interval. The upper bound of the variable θ, sets the following upper bound for the control input v_x,

$$v_x \leq \frac{-k_1 + \sqrt{{k_1}^2 + 4k_2\ m\ g\ tan(\theta_{max})}}{2k_2}, \tag{146}$$

and the lower bound is found analogously. This result together with the fact the $F(\theta)$ is bijective in the valid interval, finishes the proof. □

Definition 3. *The minimum-energy problem is the optimal control problem described in (137) or (138) for the case when the cost index C_I is equal to zero.*

Theorem 4.1. *The solution of the minimum-energy problem is given by the following*

$$\theta^* = \begin{cases} \theta_{crit}\ ,\ \theta_{crit} < \theta_{max} \\ \theta_{max}\ ,\ \theta_{crit} \geq \theta_{max}. \end{cases} \tag{147}$$

where $\theta_{crit} \in (0, \pi/2)$ is

$$\theta_{crit} = tan^{-1}\left(\frac{k_1 v_{x_{crit}} + k_2 v_{x_{crit}}^2}{mg} \right), \tag{148}$$

and the value of the forward flight speed $v_{x_{crit}}$ at the critical point is the only real positive root of the quartic polynomial

$$p(v_x) = 4k_2^2 v_x^4 + 5k_1 k_2 v_x^3 + k_1^2 v_x^2 - 2(mg)^2. \tag{149}$$

Proof. Because v_x is constant it is possible to write the final time integrating $\dot{x}$, which yields $t_f = \frac{x_f}{v_x}$. Since the integrand of the cost functional J is constant in time, it is possible to write,

$$J = \left(CI + ((k_1 v_x + k_2 v_x^2)^2 + (mg)^2)^{3/4} \right) \frac{x_f}{v_x}. \tag{150}$$

Since $C_I = 0$, the necessary condition is,

$$J_{v_x} = \left(\frac{v_x^2(k_1^2 + 5k_1 k_2 v_x + 4k_2^2 v_x^2) - 2(mg)^2}{2v_x^2(v_x^2(k_1 + k_2 v_x)^2 + (mg)^2)^{1/4}} \right) x_f = 0, \tag{151}$$

which, for $v_x > 0$, $k_1 > 0$, $k_2 > 0$, $mg > 0$, implies that

$$v_x^2(k_1^2 + 5k_1 k_2 v_x + 4k_2^2 v_x^2) - 2(mg)^2 = 0. \tag{152}$$

The study of the roots of the polynomial in (152) can be found in Appendix A.2. The only possible configurations of roots are: two real roots and two complex conjugate non-real roots, or four real roots. Because of the Descartes' rule of signs for a single-variable polynomial with real coefficients, the maximum number of positive roots of (152) is one, and the allowed number of negative roots are three or one. Therefore, only one real positive solution exists, and the pitch angle at the critical point is obtained from (141).

The sufficient condition for a minimum can be verified as follows. Let J in (150) be written in the fraction format $J = N/D$, where $N = \left(CI + ((k_1 v_x + k_2 v_x^2)^2 + (mg)^2)^{3/4}\right) x_f$ and $D = v_x$. The second partial derivative of J with respect to v_x is then,

$$J_{v_x v_x} = \frac{N_{v_x v_x} - 2J_{v_x} D_{v_x} - J D_{v_x v_x}}{D}. \tag{153}$$

One can straightforwardly compute the partial derivates of N with respect to v_x,

$$N_{v_x} = \frac{3v_x(k_1 + k_2 v_x)(k_1 + 2k_2 v_x)}{2\sqrt[4]{(k_1 v_x + k_2 v_x^2)^2 + (mg)^2}} x_f, \tag{154}$$

$$N_{v_x v_x} = \frac{3(k_1^2 v_x^2 + 10k_1^3 k_2 v_x^3 + k_1^2(25k_2^2 v_x^4 + 2(mg)^2)}{4((k_1 v_x + k_2 v_x^2)^2 + (mg)^2)^{5/4}} x_f + \frac{3k_1 k_2 v_x(2k_2^2 v_x^4 + (mg)^2) + 2k_2^4 v_x^6 + 3k_2^2 v_x^2 (mg)^2)}{((k_1 v_x + k_2 v_x^2)^2 + (mg)^2)^{5/4}} x_f > 0 \tag{155}$$

At the critical point $v_{x_{crit}}$, the second term of (153) vanishes to satisfy the necessary condition in (151), i.e., $J_{v_x}(v_{x_{crit}}) = 0$. In conclusion, since $D_{v_x v_x} = 0$ and $D > 0$,

$$J_{v_x v_x}(v_{x_{crit}}) = \frac{N_{v_x v_x}}{D} > 0, \tag{156}$$

which completes the proof. □

Remark 8. *Note that if the necessary condition is satisfied, the sufficient condition is fulfilled regardless of C_I.*

Corollary 4.1.1. *Multiplying the drag coefficients and the mass by the same factor δ does not change the solution (147).*

Proof. The polynomial in (149) becomes,

$$p(v_x) = 4k_2^2 \delta^2 v_x^4 + 5k_1 k_2 \delta^2 v_x^3 + k_1^2 \delta^2 v_x^2 - 2(mg)^2 \delta^2, \tag{157}$$

which has the same roots of (149). Moreover,

$$\theta_{crit} = tan^{-1}\left(\frac{k_1 \delta v_{x_{crit}} + k_2 \delta v_{x_{crit}}^2}{m\delta g}\right) = tan^{-1}\left(\frac{k_1 v_{x_{crit}} + k_2 v_{x_{crit}}^2}{mg}\right). \tag{158}$$

□

4.2.2 General Economy Mode

The subsection studies the general economy mode problem, i.e. $C_I \geq 0$

Proposition 4.2. *Under the assumptions (4.1-4.9), there is at least one minimizer θ_{crit} satisfying the equation*

$$\frac{d\,G(\theta_{crit})}{d\theta}F(\theta_{crit}) = G(\theta_{crit})\frac{d\,F(\theta_{crit})}{d\theta}, \qquad 0 < \theta_{crit} < \frac{\pi}{2} \tag{159}$$

Proof. For the steady forward flight configuration, $G(\theta)$, $F(\theta)$, and θ do not depend on time, since $\ddot{x} = 0$. One can write the following expression for the final time by integrating (137),

$$t_f = \frac{x_f}{F(\theta)}. \tag{160}$$

The cost functional is then

$$J = \int_0^{\frac{x_f}{F(\theta)}} G(\theta)d\tau = G(\theta)\frac{x_f}{F(\theta)}. \tag{161}$$

A necessary condition of optimality is

$$J_\theta = \frac{G_\theta(\theta)F(\theta) - G(\theta)F_\theta(\theta)}{F^2(\theta)}x_f = 0. \tag{162}$$

Since sines and cosines are positive in the first quadrant, the following statements are true for $\theta \in (0, \pi/2)$.

$$G(\theta) = C_I + \left(\frac{mg}{cos(\theta)}\right)^{3/2} > 0,$$

$$G_\theta(\theta) = \frac{3(mg)^{3/2}sin(\theta)}{2cos(\theta)^{5/2}} > 0,$$

$$F(\theta) = \frac{-k_1 + \sqrt{{k_1}^2 + 4k_2\ m\ g\ tan(\theta)}}{2k_2} > 0,$$

$$F_\theta(\theta) = \frac{mg\ sec^2\theta}{\sqrt{{k_1}^2 + 4k_2\ mg\ tan(\theta)}} > 0$$

Additionally,

$$\lim_{\theta\to 0^+} G(\theta) = C_I + (mg)^{3/2}$$

$$\lim_{\theta\to 0^+} G_\theta(\theta) = 0,$$

$$\lim_{\theta\to 0^+} F(\theta) = 0,$$

$$\lim_{\theta\to 0^+} F_\theta(\theta) = \frac{mg}{k_1},$$

and because

$$\lim_{\theta\to 0^+} F^2(\theta) = 0, \tag{163}$$

we have

$$\lim_{\theta\to 0^+} J_\theta(\theta) = -\infty. \tag{164}$$

Similarly, it is possible to verify that

$$\lim_{\theta\to \frac{\pi}{2}^-} G(\theta) = +\infty,$$

$$\lim_{\theta\to \frac{\pi}{2}^-} F(\theta) = +\infty,$$

therefore l'Hôpital's rule can be applied in order to find $\lim_{\theta\to \frac{\pi}{2}^-} J(\theta)$,

$$\lim_{\theta\to \frac{\pi}{2}^-} J(\theta) = \lim_{\theta\to \frac{\pi}{2}^-} \frac{G(\theta)}{F(\theta)} = \lim_{\theta\to \frac{\pi}{2}^-} \frac{F_\theta(\theta)}{G_\theta(\theta)} = \frac{3(mg)^{1/2} sin(\theta)\sqrt{{k_1}^2 + 4k_2\, mg\, tan(\theta)}}{2cos(\theta)^{1/2}} = +\infty. \tag{165}$$

Since J is continuous, it is bounded for any closed and bounded interval $[a, b] \subset (0, \pi/2)$. Thus because of (165), J increases somewhere in the interval $(b, \pi/2)$, i.e., J_θ is positive somewhere in this interval. Note that one can make b as close to $\pi/2$ as one wants, yielding $\lim_{\theta\to \frac{\pi}{2}^-} J_\theta(\theta) > 0$. Furthermore because of (164), according to the intermediate value theorem, J_θ has at least one zero θ_{crit} in the interval $(0, \pi/2)$. Therefore, according to the remark 8 for the equivalent OCP in (138), every zero of J_θ is a minimizer of J.

□

Corollary 4.1.2. *When $k_2 = 0$, $\theta_{crit} = arccos(\beta_{crit}^2)$, where β_{crit} is the only real root of the quartic polynomial,*

$$p(\beta) = \beta^4 + \left(\frac{2}{3} C_I (mg)^{-3/2}\right)\beta^3 - \frac{1}{3} \tag{166}$$

Proof. The forward flight speed function reduces to $\lim_{k_2 \to 0} F(\theta) = mg\ tan(\theta)/k_1$, which can be shown using l'Hôpital's rule. Expression (159) is

$$\left(\frac{3(mg)^{3/2} sin(\theta_{crit})}{2cos(\theta_{crit})^{5/2}}\right)\left(\frac{mg\ tan(\theta_{crit})}{k_1}\right) = \left(C_I + \left(\frac{mg}{cos(\theta_{crit})}\right)^{3/2}\right)\left(\frac{mg}{k_1 cos^2(\theta_{crit})}\right) \tag{167}$$

which, using the trigonometric substitutions detailed in Appendix A.3, can be reduced to

$$cos^2(\theta_{crit}) + \frac{2}{3} C_I mg^{-3/2} cos(\theta_{crit})^{3/2} - \frac{1}{3} = 0. \tag{168}$$

The replacement of the variable $\beta = cos(\theta)^{1/2}$ in (168) yields the polynomial (166) defined in the corollary. The discriminant (defined in Appendix A.2) of the polynomial $p(\beta)$ is negative, therefore, because of the Descartes' rule of signs, a unique real positive solution is guaranteed, which finishes the proof. □

Remark 9. *The condition established in Corollary 4.1.2 shows that the critical pitch angle θ_{crit} does not depend on the drag coefficient k_1.*

Remark 10. *The critical pitch angle θ_{crit} of Corollary 4.1.2 for the minimum energy case ($C_I = 0$) is the first quadrant root of a second-order Legendre polynomial $P_2(cos\theta)$, also known as the magic angle, which is $\theta_m = arccos(1/\sqrt{3})$ or approximately 54.7356^o [63].*

Corollary 4.1.3. *When $k_1 = 0$, $\theta_{crit} = arccos(\beta_{crit}^2)$, where β_{crit} is the only real root of the quartic polynomial*

$$p(\beta) = \beta^4 + \left(\frac{1}{3} C_I (mg)^{-3/2}\right)\beta^3 - \frac{2}{3} \tag{169}$$

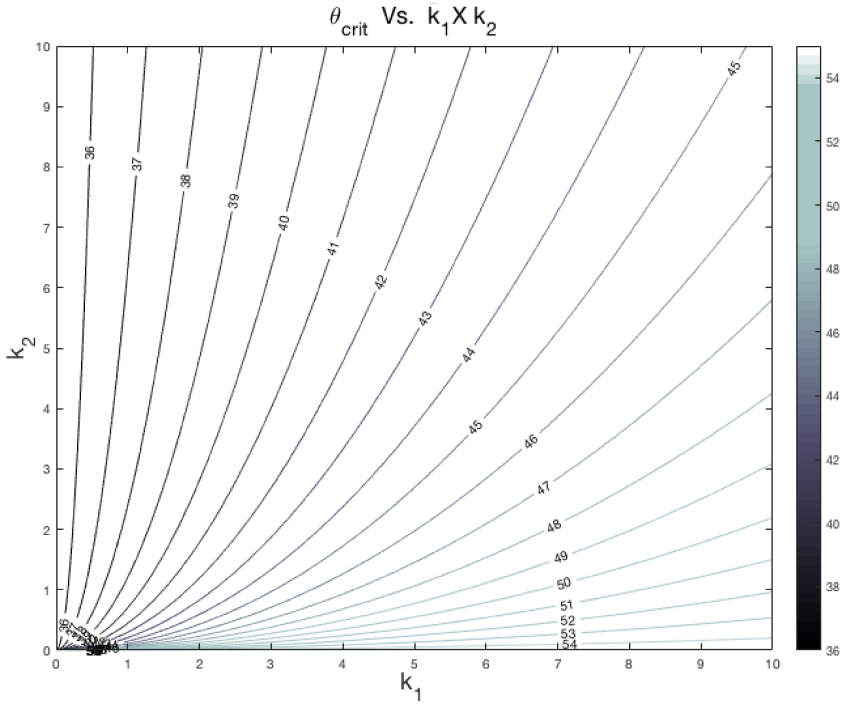

Figure 4.2: Contour curves of critical angle θ_{crit} against drag parameters k_1 and k_2.

Proof. When $k_1 = 0$, the forward flight speed function reduces to $F(\theta) = \sqrt{\frac{mg\ tan(\theta_{crit})}{k_2}}$. Expression (159) becomes

$$\left(\frac{3(mg)^{3/2}sin(\theta_{crit})}{2cos(\theta_{crit})^{5/2}}\right)\sqrt{\frac{mg\ tan(\theta_{crit})}{k_2}} = \left(C_I + \left(\frac{mg}{cos(\theta_{crit})}\right)^{3/2}\right)\left(\frac{\sqrt{mg}}{2\sqrt{k_2\ tan(\theta_{crit})}cos^2(\theta_{crit})}\right) \tag{170}$$

which can be simplified into (see Appendix A.4),

$$cos^2(\theta_{crit}) + \frac{1}{3}C_I mg^{-3/2}cos(\theta_{crit})^{3/2} - \frac{2}{3} = 0. \tag{171}$$

The replacement of the variable $\beta = cos(\theta)^{1/2}$ into (171) yields the polynomial (169) defined in the corollary. The discriminant of the polynomial $p(\beta)$ is negative, therefore, because of the Descartes' rule of signs for a single-variable polynomial with real coefficients, a unique real positive solution is guaranteed, which finishes the proof. □

Remark 11. *The condition established in Corollary 4.1.3 shows that the critical pitch angle* θ_{crit}

does not depend on the drag coefficient k_2.

Remark 12. *The critical pitch angle θ_{crit} of Corollary 4.1.3 for the minimum energy case ($C_I = 0$) is the first quadrant root of a second-order Legendre polynomial $P_2(sin\theta)$, also known as the complementary magic angle, which is $\overline{\theta}_m = arcsin(1/\sqrt{3})$ or approximately 35.2644^o.*

Conjecture 4.1. *For m of the order of practical UAV masses, the critical pitch angle θ_{crit} for the minimum energy case ($C_I = 0$) lies inside the interval*

$$\overline{\theta}_m \leq \theta_{crit} \leq \theta_m \tag{172}$$

for any positive values of k_1 and k_2.

The above conjecture comes from an empirical study of the possible solutions. It is clear from Theorem 4.2 that the critical angle θ_{crit} does not depend on the final position x_f. Additionally, if g is considered to be constant, the only remaining variable parameters of OCP (137) are k_1, k_2, and m. The values of k_1 and k_2 for are generally less than 1. Figure 4.2 shows the the contour curve of θ_{crit} against the plane $k_1 \times k_2$, with $0 \leq k_1 \leq 10$, and $0 \leq k_2 \leq 10$ (overdimensioned values for real applications), for a quadrotor mass of 0.71 Kg. Figure 4.3 shows the manifold of solutions for $m = 0.3Kg$, $3.0Kg$, and $30.0Kg$. As one can conclude, no solution outside of the interval $\overline{\theta}_m \leq \theta_{crit} \leq \theta_m$ was found.

4.3 Maximum Range Optimal Control Problem

In this section, the maximum range Optimal Control Problem (OCP) for the longitudinal forward flight of a quadcopter is formulated. The objective is to maximize the total distance (or final position)

$$x_f = \int_0^{t_f} \dot{x}\, d\tau \tag{173}$$

considering that $x(0) = 0$. Similarly to the previous section, the maximum range OCP can then be stated as

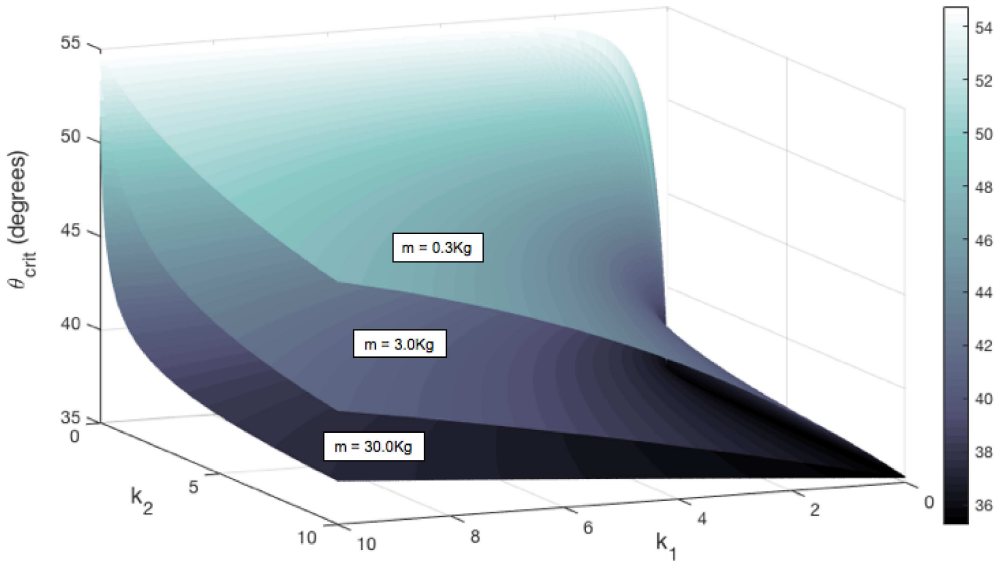

Figure 4.3: Critical angle solution manifolds.

Figure 4.4: Asctec Pelican quadrotor

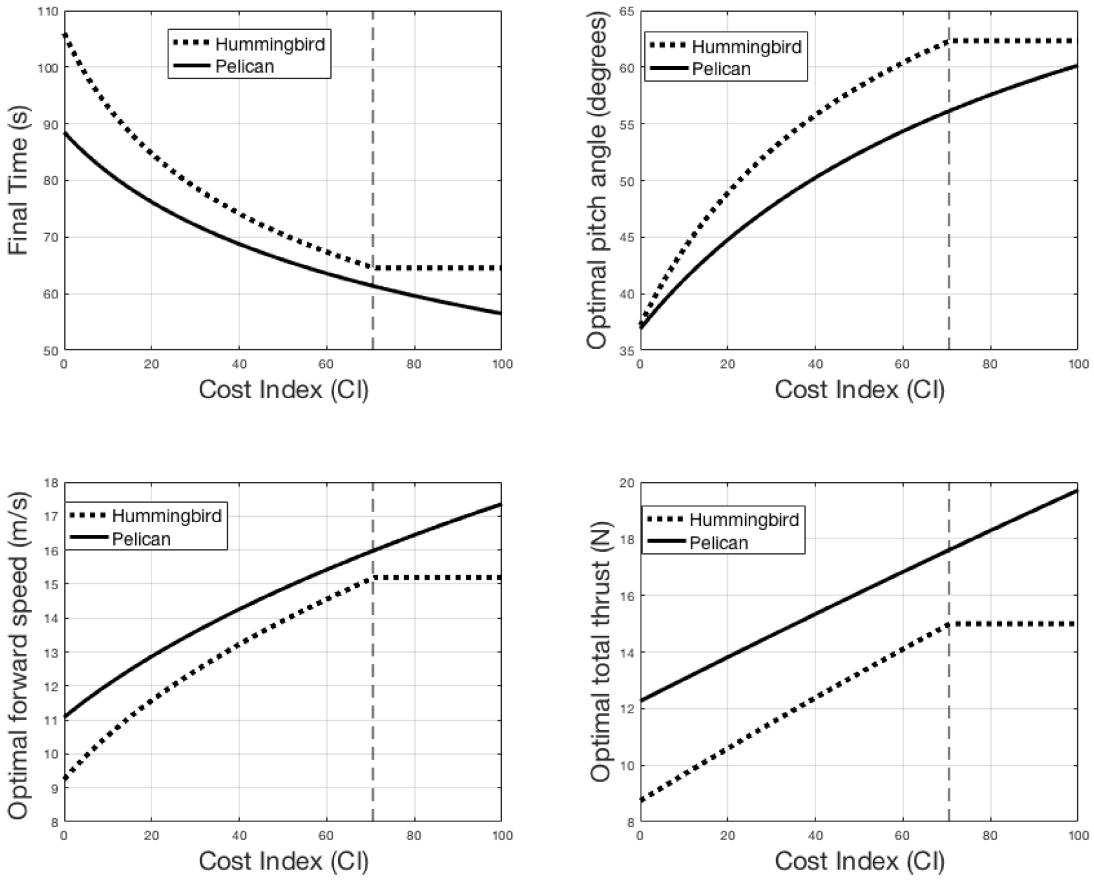

Figure 4.5: Economy mode solution against C_I

$$\begin{aligned} \max_{\theta, t_f} \; & J = \int_0^{t_f} F(\theta) d\tau \\ & s.t. \\ \dot{q} = H(\theta) = & -\frac{\zeta}{2\eta U}\left(\frac{mg}{cos(\theta)}\right)^{3/2}, \\ & \dot{v_x} = 0, \\ & q(0) = Q_o, q(t_f) = 0, \\ & 0 < \theta \leq \theta_{max} < \pi/2 \end{aligned} \tag{174}$$

where $F(\theta) = \frac{-k_1 + \sqrt{{k_1}^2 + 4k_2 \; m \; g \; tan(\theta)}}{2k_2}$, Q_o is the initial battery charge, and the final time t_f is free. The limit θ_{max} is defined in equation (136).

Proposition 4.3. *The OCP stated in (137) reduces to (174) if $C_I = 0$ (minimum energy problem).*

Proof. For the steady forward flight configuration, the function $H(\theta)$ does not depend on time, since θ is constant as previously explained. Therefore, the integration of $H(\theta)$ with respect to time yields the following expression for the final time

$$t_f = \frac{Q_o}{H(\theta)}. \tag{175}$$

Because $F(\theta)$ is constant in time, the cost functional can be written as

$$J = \int_0^{\frac{Q_o}{H(\theta)}} F(\theta) d\tau = F(\theta) \frac{Q_o}{H(\theta)}. \tag{176}$$

A necessary condition of optimality is

$$J_\theta = \frac{F_\theta(\theta_{crit}) H(\theta_{crit}) - F(\theta_{crit}) H_\theta(\theta_{crit})}{H^2(\theta_{crit})} Q_o = 0. \tag{177}$$

Since, for $C_I = 0$, one can transform $H(\theta)$ into $G(\theta)$ times a constant, the solutions of equation (177) correspond to the solutions of equation (162), which finishes the proof. □

4.4 Simulations

This section presents the results of simulations for the quadrotor economy mode solution developed in the previous sections.

Table 4.1: Quadrotor parameters

	Hummingbird	**Pelican**
Mass m	0.71 kg	1.00 kg
Propeller size d	20,32 cm	25,40 cm
LiPo battery capacity Q_o	2100 mAh	6250 mAh
Battery voltage $U_{nominal}$	11.1 V	11.1 V
Max Thrust	15 N	36 N
Endurance	up to 15 min	up to 30 min
Max motor power	4 x 80 W	4 x 160 W

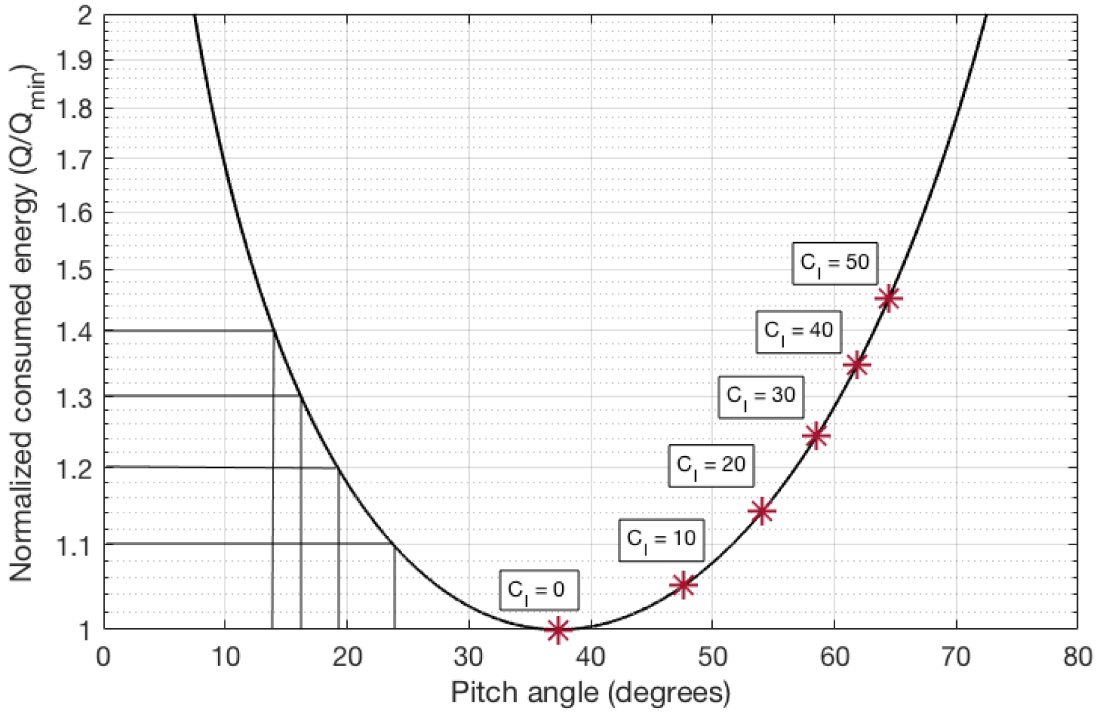

Figure 4.6: Normalized consumed energy against pitch angles

4.4.1 Quadrotor Model

The Asctec Hummingbird and Pelican quadrotor models are used in the following simulations (see Figures 3.3 and 4.4). Table 4.1 shows the quadrotor model parameters adopted in the simulations. The electromechanical conversion efficiency (η) is considered to be 0.75 for both quadrotor models. The air density is considered to be $\rho = 1.225\ kg/m^3$ (approximately sea level altitude), and the gravitational acceleration is $g = 9.81\ m/s^2$. Furthermore, the ratio $\frac{C_M}{d\sqrt{{C_T}^3}}$ is considered to be the same for the two quadrotors, leading to $\zeta = 14.37\ m^2/kg$.

4.4.2 Economy Mode

As stated in the previous section the cost index C_I comprises both the aerodynamic effects of the propellers and the time-related and battery costs. This variable becomes then the crucial element of the flight management system. The optimal pitch angle, total thrust, total time, and forward speed for the two quadrotors are plotted against the cost index C_I in the Figure 4.5. The dashed lines represent the saturation point (maximum allowed total thrust) of the solution for the Hummingbird

quadrotor. In these simulations, the drag coefficients are considered to be $k_1 = 0.100kg/s$, and $k_2 = 0.051kg/(m.s)$ for both UAVs. In addition, the final position (x_f) is set to $100m$. It can be seen that higher cost indices imply shorter flight times, larger pitch angles, requiring higher thrusts.

Figure 4.6 shows the normalized consumed charge (Q/Q_{min}) versus the chosen pitch angle, where Q_{min} is the optimal consumed charge when $C_I = 0$. In this simulation, $k_1 = 0.100kg/s$ and $k_2 = 0.051kg/(m.s)$, which yielded an angle of 36.7418^o for $C_I = 0$. It is possible to see from the plot how pitch angle displacements affect the consumed charge. Values where the consumed energy increases by 10%, 20%, 30%, and 40% regarding the optimal solution are denoted by solid lines. Optimal pitch angles for different values of C_I are shown in red. Higher cost indices lead to higher charge consumptions and conversely to faster trajectories. For instance, the case where $C_I = 50$ spends 45.46% more charge than the minimum-energy case, whereas it is 41.59% faster.

Chapter 5

Conclusions and Future Work

5.1 Conclusions

This thesis addressed the problem of trajectory planning for a quadrotor UAV on the longitudinal plane. Energy-based algorithms for the trajectory generation problem were proposed.

An optimal state feedback solution, in the sense of the trade-off between body accelerations and total flight time, that considers the nonlinearities of the quadrotor's equations of motion and the drag force components were developed in Chapter 3, addressing the case of short trajectories. This solution was derived using the Pontryagin's Minimum Principle (PMP). Simulations showed the suitability of the proposed method. In order to consider the nonlinearities of the system, Chapter 3 proposes a change of variables that leads to a linear formulation of the two-point boundary value problem. The main advantage of this technique is that it provides a state-feedback analytical expression, which is a key feature for real-time trajectory planning, especially considering limited onboard CPU capabilities for small vehicles. In this framework, the trade-off mentioned above is parametrized by the cost index (C_I). The methodology can handle both system nonlinearities and drag effect. Results from simulations show how the trade-off coefficient can be used to address the control energy/time trade-off. Besides, the drag effect demands extra energy for accomplishing the goal. As a result, the system operates at extremum pitch angle and thrust for longer and the maximum allowed optimal velocity magnitudes are reduced according to the drag effect.

To address the case of long trajectories, Chapter 4 presented the derivation of a quadcopter

power consumption model using blade element momentum theory. The power consumption model was put into the optimal control problem framework in order to formulate the economy mode problem subject to constraints. An analytical solution for the constant altitude steady state flight economy mode problem was obtained, and it was shown to be equivalent to the maximum range problem solution. Furthermore, the geometrical bound for the optimal pitch angle in between the magic angle and its complementary angle was conjectured based on the nature of the solutions. Simulations showed how the solution behaves against several parameters.

5.2 Extensions

Several possible extensions to the work provided in this thesis include:

(1) The third component of the translational motion (y-axis) may be considered as well as the remaining rotational degrees of freedom (roll and yaw). Due to the model complexity, the 3D version of the problems formulated in this thesis will most probably require a numerical solution.

(2) A constrained version of the body accelerations and final time trade-off problem can be formulated and solved using PMP.

(3) Power terms that are more significant in fast motion, for instance, parasite power can be included.

(4) Onboard wind sensors can feed the real-time FMS trajectory planning algorithm.

(5) Non-constant electromechanical conversion efficiency can be studied.

(6) Minor mechanical losses in the rotor model, such as tip losses, wake swirl, and non-uniform inflow can be considered.

(7) A nonsteady forward flight economy mode problem can be formulated based on the power consumption power of Chapter 4, where the solution will most probably require a numerical approach.

(8) The battery dynamic model of LiPo batteries can be changed to include for non-ideal effects.

(9) The optimal control framework for trajectory planning can be extended to other types of UAVs, for instance, hexarotors, VTOLs, and hybrid UAVs.

(10) The comparison between the obtained solutions and other approaches in the literature by experimental means can also be the subject of future research.

Appendix A

A.1 Non drag equations recovery of Section 3.3

The limit when k approaches zero for the expressions obtained considering the drag influence (104) and (105) can be taken in order to recover the non-drag equations (80) and (82), respectively.

A.1.1 Velocity equation

$$\lim_{k\to 0} v_x(t) = \lim_{k\to 0}\left[\frac{J_x}{k^2}(cosh(kt)-1) - \frac{J_{v_x}(0)}{k}sinh(kt)\right], \tag{178}$$

using l'Hôpital's rule twice and knowing that $\lim_{k\to 0} cosh(kt) = 1$,

$$\lim_{k\to 0} v_x(t) = \lim_{k\to 0}\left[\frac{J_x}{2k}(t\ sinh(kt)-0) - \frac{J_{v_x}(0)}{1}t\ cosh(kt)\right], \tag{179}$$

$$\lim_{k\to 0} v_x(t) = \lim_{k\to 0}\left[\frac{J_x}{2}(t^2\ cosh(kt))\right] - J_{v_x}(0)t = \frac{J_x t^2}{2} - J_{v_x}(0)t, \tag{180}$$

which is equal to (80) when $v_{x_0} = 0$.

A.1.2 Position equation

$$\lim_{k\to 0} x(t) = \lim_{k\to 0}\left[x_0 + \frac{J_x}{k^3}(sinh(kt)-kt) - \frac{J_{v_x}(0)}{k^2}(cosh(kt)-1)\right], \tag{181}$$

applying l'Hôpital's rule consecutively,

$$\lim_{k\to 0} x(t) = x_0 + \lim_{k\to 0}\left[\frac{J_x}{3k^2}(t\ cosh(kt) - t) - \frac{J_{v_x}(0)}{2k}(t\ sinh(kt) - 0)\right], \tag{182}$$

$$\lim_{k\to 0} x(t) = x_0 + \lim_{k\to 0}\left[\frac{J_x}{6k}(t^2\ sinh(kt) - 0) - \frac{J_{v_x}(0)}{2}(t^2\ cosh(kt))\right], \tag{183}$$

$$\lim_{k\to 0} x(t) = x_0 + \lim_{k\to 0}\left[\frac{J_x}{6}(t^3\ cosh(kt))\right] - \frac{J_{v_x}(0)}{2}t^2 = x_0 + \frac{J_x}{6}t^3 - \frac{J_{v_x}(0)}{2}t^2, \tag{184}$$

which is equal to (82) when $v_{x_0} = 0$.

A.2 Proposition 4.1 - Quartic polynomial study

For the complete solution of quartic polynomials the reader is referred to [64]. The nature of the roots of a quartic polynomial $a\beta^4 + b\beta^3 + c\beta^2 + d\beta + e = 0$ with real coefficients (a, b, c, d, e) can be determined by the sign of the following auxiliary polynomials.

(1) *Discriminant*:

$$\begin{aligned}\Delta_4 \ &= 256a^3e^3 - 192a^2bde^2 - 128a^2c^2e^2 + 144a^2cd^2e - 27a^2d^4 \\ &\quad + 144ab^2ce^2 - 6ab^2d^2e - 80abc^2de + 18abcd^3 + 16ac^4e \\ &\quad - 4ac^3d^2 - 27b^4e^2 + 18b^3cde - 4b^3d^3 - 4b^2c^3e + b^2c^2d^2\end{aligned} \tag{185}$$

(2) $P = 8ac - 3b^2$

(3) $R = b^3 + 8da^2 - 4abc$

(4) $D = 64a^3e - 16a^2c^2 + 16ab^2c - 16a^2bd - 3b^4$

(5) $\Delta_0 = c^2 - 3bd + 12ae$

Proposition 4.1 leads to the following polynomial,

$$v_x^2(k_1^2 + 5k_1k_2v_x + 4k_2^2v_x^2) - 2(mg)^2 = 0 \tag{186}$$

with $k_1 > 0$, $k_2 > 0$, and $mg > 0$. The discriminant of the quartic polynomial (186) is

$$\Delta_4 = -4k_2^2(mg)^2[32768k_2^4(mg)^4 + 4523k_1^4k_2^2(mg)^2 - 18k_1^8] \tag{187}$$

which *a priori* can be negative, positive or zero. The following auxiliary polynomials of this specific quartic form are:

(1) $P = -43k_1^2k_2^2 < 0$

(2) $R = 45k_1^3k_2^3 > 0$

(3) $D = -8192k_2^6(mg)^2 - 531k_1^4k_2^4 < 0$

(4) $\Delta_0 = -96k_2^2(mg)^2 + k_1^4$

The following possible sets of roots are listed.

(1) $\Delta_4 < 0$: two distinct real roots and two complex conjugate non-real roots.

(2) $\Delta_4 > 0$: four real roots and distinct since $P < 0$ and $D < 0$.

(3) $\Delta_4 = 0$:

$\Delta_0 \neq 0$: a real double root and two real simple roots since $P < 0$ and $D < 0$.

$\Delta_0 = 0$: triple real root and a simple real root since $D \neq 0$.

In conclusion, every possible set of roots listed above can be grouped into one of the two: two real roots and two complex conjugate non-real roots (if $\Delta_4 < 0$), four real roots otherwise.

A.3 Corollary 4.1.2 step-by-step equation

Starting with the following expression,

$$\left(\frac{3(mg)^{3/2}sin(\theta_{crit})}{2cos(\theta_{crit})^{5/2}}\right)\left(\frac{mg\tan(\theta_{crit})}{k_1}\right) = \left(C_I + \left(\frac{mg}{cos(\theta_{crit})}\right)^{3/2}\right)\left(\frac{mg}{k_1cos^2(\theta_{crit})}\right),$$

dividing both sides by $\frac{mg}{k_1}$

$$\left(\frac{3(mg)^{3/2}sin(\theta_{crit})}{2cos(\theta_{crit})^{5/2}}\right)\tan(\theta_{crit}) = \left(C_I + \left(\frac{mg}{cos(\theta_{crit})}\right)^{3/2}\right)\left(\frac{1}{cos^2(\theta_{crit})}\right),$$

replacing $\tan(\theta_{crit}) = \frac{sin(\theta_{crit})}{cos(\theta_{crit})}$, and multiplying both sides by $cos^2(\theta_{crit})$

$$\left(\frac{3(mg)^{3/2}sin(\theta_{crit})}{2cos(\theta_{crit})^{3/2}}\right)sin(\theta_{crit}) = \left(C_I + \left(\frac{mg}{cos(\theta_{crit})}\right)^{3/2}\right),$$

dividing both sides by $\frac{(mg)^{3/2}}{cos(\theta_{crit})^{3/2}}$

$$\frac{3}{2}sin^2(\theta_{crit}) = C_I mg^{-3/2}cos(\theta_{crit})^{3/2} + 1,$$

since $sin^2(\theta_{crit}) = 1 - cos^2(\theta_{crit})$

$$\frac{3}{2} - \frac{3}{2}cos^2(\theta_{crit}) = C_I mg^{-3/2}cos(\theta_{crit})^{3/2} + 1,$$

dividing both sides by $3/2$ and rearranging, yields our final expression

$$cos^2(\theta_{crit}) + \frac{2}{3}C_I mg^{-3/2}cos(\theta_{crit})^{3/2} - \frac{1}{3} = 0.$$

A.4 Corollary 4.1.3 step-by-step equation

Starting with the expression

$$\left(\frac{3(mg)^{3/2}sin(\theta_{crit})}{2cos(\theta_{crit})^{5/2}}\right)\sqrt{\frac{mg\tan(\theta_{crit})}{k_2}} = \left(C_I + \left(\frac{mg}{cos(\theta_{crit})}\right)^{3/2}\right)\left(\frac{\sqrt{mg}}{2\sqrt{k_2\,tan(\theta_{crit})}cos^2(\theta_{crit})}\right),$$

dividing both sides by $\sqrt{\frac{mg}{k_2}}$

$$\left(\frac{3(mg)^{3/2}sin(\theta_{crit})}{2cos(\theta_{crit})^{5/2}}\right)\sqrt{\tan(\theta_{crit})} = \left(C_I + \left(\frac{mg}{cos(\theta_{crit})}\right)^{3/2}\right)\left(\frac{}{2\sqrt{\tan(\theta_{crit})}cos^2(\theta_{crit})}\right),$$

multiplying both sides by $2\sqrt{\tan(\theta_{crit})}cos^2(\theta_{crit})$

$$\left(\frac{3(mg)^{3/2}sin(\theta_{crit})}{cos(\theta_{crit})^{1/2}}\right)\tan(\theta_{crit}) = \left(C_I + \left(\frac{mg}{cos(\theta_{crit})}\right)^{3/2}\right),$$

replacing $\tan(\theta_{crit}) = \frac{sin(\theta_{crit})}{cos(\theta_{crit})}$, and dividing both sides by $\frac{(mg)^{3/2}}{cos(\theta_{crit})^{3/2}}$

$$3sin^2(\theta_{crit}) = C_I mg^{-3/2}cos(\theta_{crit})^{3/2} + 1$$

since $sin^2(\theta_{crit}) = 1 - cos^2(\theta_{crit})$

$$3 - 3cos^2(\theta_{crit}) = C_I mg^{-3/2}cos(\theta_{crit})^{3/2} + 1$$

finally, rearranging and dividing by 3

$$cos^2(\theta_{crit}) + \frac{1}{3}C_I mg^{-3/2}cos(\theta_{crit})^{3/2} - \frac{2}{3} = 0.$$

Bibliography

[1] C. N. Adkins and R. H. Liebeck, "Design of optimum propellers," Journal of Propulsion and Power, vol. 10, no. 5, pp. 676–682, 1994.

[2] B. Theys, G. Dimitriadis, P. Hendrick, and J. De Schutter, "Influence of propeller configuration on propulsion system efficiency of multi-rotor unmanned aerial vehicles," in Unmanned Aircraft Systems (ICUAS), 2016 International Conference on. IEEE, 2016, pp. 195–201.

[3] M. Achtelik, K.-M. Doth, D. Gurdan, and J. Stumpf, "Design of a multi rotor mav with regard to efficiency, dynamics and redundancy," in AIAA Guidance, Navigation, and Control Conference, 2012, p. 4779.

[4] J. A. Benito, G. Glez-de Rivera, J. Garrido, and R. Ponticelli, "Design considerations of a small uav platform carrying medium payloads," in Design of Circuits and Integrated Circuits (DCIS), 2014 Conference on. IEEE, 2014, pp. 1–6.

[5] D. Aleksandrov and I. Penkov, "Energy consumption of mini uav helicopters with different number of rotors," in 11th International Symposium" Topical Problems in the Field of Electrical and Power Engineering, 2012, pp. 259–262.

[6] S. B. A. Abdilla, A. Richards, "Power and endurance modelling of battery-powered rotorcraft," in IEEE/RSJ International Conference on Intelligent Robots and Systems (IROS), 2015.

[7] Y. Mulgaonkar, M. Whitzer, B. Morgan, C. M. Kroninger, A. M. Harrington, and V. Kumar, "Power and weight considerations in small, agile quadrotors," in Micro-and Nanotechnology Sensors, Systems, and Applications VI, vol. 9083. International Society for Optics and Photonics, 2014, p. 90831Q.

[8] M. C. Achtelik, J. Stumpf, D. Gurdan, and K.-M. Doth, "Design of a flexible high performance quadcopter platform breaking the mav endurance record with laser power beaming," in Intelligent robots and systems (iros), 2011 ieee/rsj international conference on. IEEE, 2011, pp. 5166–5172.

[9] D. Lee, J. Zhou, and W. T. Lin, "Autonomous battery swapping system for quadcopter," in Unmanned Aircraft Systems (ICUAS), 2015 International Conference on. IEEE, 2015, pp. 118–124.

[10] J. Verbeke, D. Hulens, H. Ramon, T. Goedeme, and J. De Schutter, "The design and construction of a high endurance hexacopter suited for narrow corridors," in Unmanned Aircraft Systems (ICUAS), 2014 International Conference on. IEEE, 2014, pp. 543–551.

[11] A. Miele, "A survey of the problem of optimizing flight paths of aircraft and missiles," Mathematical Optimization Techniques, pp. 3–32, 1963.

[12] T. Rivers, "Design and integration of a flight management system for the unmanned air vehicle frog," Master's thesis, Naval Postgraduate School, Monterey, 1998.

[13] K. Eliker, H. Bouadi, and M. Haddad, "Flight planning and guidance features for an uav flight management computer," in IEEE Emerging Technologies and Factory Automation (ETFA), 2016.

[14] A. Tarhan and et al., "Formal intent based flight management system design for unmanned aerial vehicles," in IEEE Unmanned Aircraft Systems (ICUAS), 2014.

[15] Y. Bouktir, M. Haddad, and T. Chettibi, "Trajectory planning for a quadrotor helicopter," in IEEE 16th Mediterranean Conference on Control and Automation, 2008.

[16] E. Kahale, P. Castillo, and Y. Bestaoui, "Minimum time reference trajectory generation for an autonomous quadrotor," in Unmanned Aircraft Systems (ICUAS), 2014 International Conference on. IEEE, 2014, pp. 126–133.

[17] R. Ritz and et al., "Quadrocopter performance benchmarking using optimal control," in Proc. Int. Conf. Intelligent Robots and Systems, 2011.

[18] D. Mellinger and V. Kumar, "Minimum snap trajectory generation and control for quadrotors," in International Conference on Robotics and Automation. Shanghai: IEEE, 2011.

[19] C. Richter, A. Bry, , and N. Roy, "Polynomial trajectory planning for aggressive quadrotor flight in dense indoor environments," in International Symposium of Robotics Research, 2013.

[20] I. Palunko, R. Fierro, and P. Cruz, "Trajectory generation for swing- free maneuvers of a quadrotor with suspended payload: A dynamic programming approach," in International Conference on Robotics and Automation, May 2012.

[21] L. Singh and J. Fuller, "Trajectory generation for a uav in urban terrain, using nonlinear mpc," in American Control Conference. IEEE, 2001.

[22] C. C. Yang, L. Lai, and C. J. Wu, "Time-optimal control of a hovering quad-rotor helicopter," Journal of Intelligent and Robotic Systems, vol. 45, no. 2, pp. 115 – 135, 2006.

[23] V. Roberge, M. Tarbouchi, and G. Labonte, "Comparison of parallel genetic algorithm and particle swarm optimization for real-time uav path planning," in International Conference on Robotics and Automation. IEEE, 2013.

[24] Safe Coordinated Maneuvering of Teams of Multirotor Unmanned Aerial Vehicles, vol. 36, 2016.

[25] M. Geisert and N. Mansard, "Trajectory generation for quadrotor based systems using numerical optimal control," in International Conference on Robotics and Automation, Sweden, 2016.

[26] Time-Critical Cooperative Control of Multiple Autonomous Vehicles, vol. 32, 2012.

[27] K. Vicencio, T. Korras, and K. Bordigon, "Energy-optimal path planning for six-rotors on multi-target missions," in Intelligent Robots and Systems (IROS). IEEE, 2015.

[28] A. Candido, R. Galvao, and T. Yoneyama, "Control and energy management for quadrotor," in ICC, UK, 2014.

[29] Y. Zeng and R. Zhang, "Energy-efficient uav communication with trajectory optimization," IEEE Trans. Wireless Commun, vol. 16, no. 6, pp. 3747–3760, 2017.

[30] M. Di Perna, "An optimal control approach to flight management systems for unmanned aerial vehicles," Master's thesis, Concordia University, 2017.

[31] C. Molter and P. Cheng, "Propeller performance calculation for multicopter aircraft at forward flight conditions and validation with wind tunnel measurements," University of Stuttgart, Stuttgart, Germany, 2017.

[32] D. K. Phung and P. Morin, "Modeling and energy evaluation of small convertible uavs," in 2nd Workshop on Research, Education and Development of Unmanned Aerial Systems, 2013.

[33] Z. Liu, R. Sengupta, and A. Kurzhanskiy, "A power consumption model for multi-rotor small unmanned aircraft systems," in Unmanned Aircraft Systems (ICUAS), 2017 International Conference on. IEEE, 2017, pp. 310–315.

[34] F. Morbidi, R. Cano, and D. Lara, "Minimum-energy path generation for a quadrotor uav," in International Conference on Robotics and Automation. IEEE, 2016.

[35] Z. Liu and R. Sengupta, "An energy-based flight planning system for unmanned traffic management," in Systems Conference (SysCon), 2017 Annual IEEE International. IEEE, 2017, pp. 1–7.

[36] A. E. Bryson and Y. Ho, Applied Optimal Control. Publishing Company, 1983.

[37] B. Carvalho, M. D. Perna, and L. Rodrigues, "Real-time optimal trajectory generation for a quadrotor uav on the longitudinal plane,," in European Control Conference, Limassol, Cyprus, June 2018, pp. 3132–3136.

[38] M. J. Amoruso, Euler Angles and Quaternions in Six Degree of Freedom Simulations of Projectiles, Army Armament, Munitions and Chemicals Command, Picatinny Arsenal., March 1996.

[39] J. Diebel, "Representing attitude: Euler angles, unit quaternions, and rotation vectors," October 2006.

[40] S. Francesco, "Quadrotor control: modeling, nonlinear control design, and simulation," Master's thesis, KTH, Sweden, 2015.

[41] M. Bangura, "Aerodynamics and control of quadrotors," Ph.D. dissertation, Australian National University, 2017.

[42] D. C. Giancoli, Physics: Principles with applications. Pearson Higher Ed, 2013.

[43] P. Pounds, R. Mahony, J. Gresham, P. Corke, and J. M. Roberts, "Towards dynamically-favourable quad-rotor aerial robots," in Proceedings of the 2004 Australasian Conference on Robotics & Automation. Australian Robotics & Automation Association, 2004.

[44] C. Kitaplioglu, "Analysis of small-scale rotor hover performance data," 1990.

[45] A. P. French, "Newtonian mechanics," 1971.

[46] P.-J. Bristeau, P. Martin, E. Salaün, and N. Petit, "The role of propeller aerodynamics in the model of a quadrotor uav," in Control Conference (ECC), 2009 European. IEEE, 2009, pp. 683–688.

[47] W. Dong, G.-Y. Gu, X. Zhu, and H. Ding, "Modeling and control of a quadrotor uav with aerodynamic concepts," in Proceedings of World Academy of Science, Engineering and Technology, no. 77. World Academy of Science, Engineering and Technology (WASET), 2013, p. 437.

[48] S. Omari, M.-D. Hua, G. Ducard, and T. Hamel, "Nonlinear control of vtol uavs incorporating flapping dynamics," in Intelligent Robots and Systems (IROS), 2013 IEEE/RSJ International Conference on. IEEE, 2013, pp. 2419–2425.

[49] O. Gur, W. H. Mason, and J. A. Schetz, "Full-configuration drag estimation," Journal of Aircraft, vol. 47, no. 4, pp. 1356–1367, 2010.

[50] Multirotor Aerial Vehicles: Modeling, Estimation, and Control of Quadrotor, vol. 19, 2012.

[51] R. Gill and R. D'Andrea, "Propeller thrust and drag in forward flight," in Conference on Control Technology and Applications (CCTA). IEEE, 2017.

[52] L. Derafa, T. Madani, A. Benallegue, and R. D'Andrea, "Dynamic modelling and experimental identification of four rotors helicopter parameters," in International Conference on Industrial Technology. IEEE, 2006.

[53] M. Schulz and et al., "High-speed, steady flight with a quadrocopter in a confined environment using a tether," in International Conference on Intelligent Robots and Systems (IROS), 2015.

[54] M. Kaptsov and L. Rodrigues, "Electric aircraft flight management systems: economy mode and maximum endurance," American Institute of Aeronautics and Astronautics, 2017.

[55] H. J. Sussmann and J. C. Willems, "300 years of optimal control: from the brachystochrone to the maximum principle," IEEE Control Systems, vol. 17, no. 3, pp. 32–44, 1997.

[56] L. S. Pontryagin, Mathematical theory of optimal processes. Routledge, 2018.

[57] D. Liberzon, Calculus of Variations and Optimal Control Theory: A concise Introduction. Princeton University Press, 2012.

[58] L. Pontryagin and et al., The Mathematical Theory of Optimal Processes. Blaisdell Moscow, 1983.

[59] A. Technologies. Technical data - asctec hummingbird. [Online]. Available: http://www.asctec.de/en/uav-uas-drones-rpas-roav/asctec-hummingbird/

[60] A. Filippone, "Flight performance of fixed and rotary wing aircraft, 2006," Access Online via Elsevier.

[61] A. R. Bramwell, D. Balmford, and G. Done, Bramwell's helicopter dynamics. Elsevier, 2001.

[62] Y. Zeng, J. Xu, and R. Zhang, "Energy minimization for wireless communication with rotary-wing uav," arXiv preprint arXiv:1804.02238, 2018.

[63] M. Bydder, "The magic angle effect: A source of artifact, determinant of image contrast, and technique for imaging," Journal of Magnetic Resonance Imaging, pp. 290–300, 2007.

[64] G. Cardano, "1545, ars magna (the rules of algebra)," 1993.